

CYANOIRON POLYPYRIDYL SENSITIZED PHOTOANODES FOR WATER OXIDATION

A THESIS SUBMITTED TO
THE GRADUATE SCHOOL OF ENGINEERING AND SCIENCE
OF BILKENT UNIVERSITY
IN PARTIAL FULFILLMENT OF THE REQUIREMENTS FOR
THE DEGREE OF
MASTER OF SCIENCE
IN
CHEMISTRY

By
Samar Batool
January 2020

CYANOIRON POLYPYRIDYL SENSITIZED PHOTOANODES
FOR WATER OXIDATION

By Samar Batool

January 2020

We certify that we have read this thesis and that in our opinion it is fully adequate,
in scope and in quality, as a thesis for the degree of Master of Science.

Ferdi Karadař(Advisor)

Ömer Dađ

Burak Ülgüt

Aysen Yılmaz

Yavuz Dede

Approved for the Graduate School of Engineering and Science:

Ezhan Karařan
Director of the Graduate School

ABSTRACT

CYANOIRON POLYPYRIDYL SENSITIZED PHOTOANODES FOR WATER OXIDATION

Samar Batool

M.S. in Chemistry

Advisor: Ferdi Karadağ

January 2020

Dye-sensitized photoelectrochemical cells (DSPECs), which convert solar energy to hydrogen fuel via water splitting process, has markedly excelled as a multidisciplinary field in the recent years. In this context, transition metal complexes (TMCs) are employed as efficient photosensitizers because of their unique photochemical and photophysical properties. Ruthenium complexes, have frequently been preferred as both photosensitizers and water oxidation catalysts in DSPECs. However, their toxicity and preciousness have been their main disadvantages. Much research has now devoted to search for highly desirable alternatives. Hexacoordinated Fe-complexes (Fe(II)L_6), being earth abundant and chemically stable, have attracted many researchers in this respect. Unfortunately, metal-to-ligand charge transfer (3MLCT) states of Fe-complexes experience ultrafast deactivation process into metal centered (MC) states lying lower in energy with respect to MLCT states, becoming unfavorable for electron injection into TiO_2 . A fundamental approach is to destabilize these MC states by associating strong field ligands with Fe-center. Given the strong sigma-donating ability of cyanide ligand, the sensitization performance of cyanoiron polypyridyl complexes has also been investigated in earlier studies revealing excited state lifetimes much lower than desired.

Herein, my study aims to tackle this problem by assisting donor iron complex not only with electron-donating cyanide groups but also with cobalt ions that are coordinated to nitrogen atoms of cyanide ligands. For this purpose, a series of cyanoiron polypyridyl complexes with different polypyridyl groups and different number of cyanide groups were prepared. These complexes were characterized by multiple techniques including UV-Visible absorption spectroscopy (UV-Vis), Fourier transform infrared spectroscopy (ATR-FTIR), X-ray photoelectron spectroscopy (XPS), Scanning electron microscopy (SEM), and Energy

dispersive X-ray analysis (EDX).

The foundation of this thesis is mainly built on the development of dye-sensitized water oxidation photoanodes. In this study, water oxidation catalytic cobalt sites were connected to iron chromophores through cyanide bridging group affording Prussian blue layer. The effect of cyanide ligands on the rate of charge transfer has also been investigated. Various material characterizations were done to inquire about the effect of cyanide ligands and cobalt catalyst.

Photoelectrochemical studies performed on four different dye-sensitized photoanodes reveal that both the type of polypyridyl ligand and the number of cyanide groups play a critical role on the efficiency of the iron photosensitizer. The results of this study suggest that Prussian blue analogues incorporating cyano-iron polypyridyl complexes could be promising assemblies for building efficient DSPECs.

Keywords: Iron-based photosensitizers, Photosensitizer-water oxidation catalyst dyad, Water splitting, Prussian blue analogues, Photoelectrochemical water oxidation.

ÖZET

SU OKSİDASYONU İÇİN SİYANODEMİR POLİPRİDİL DUYARLI FOTOANODLAR

Samar Batool

Kimya, Yüksek Lisans

Tez Danışmanı: Ferdi Karadaş

Ocak 2020

Suyu ayırma işlemi ile güneş enerjisini hidrojen yakıtına dönüştüren, boyaya duyarlı fotoelektrokimyasal hücreler son yıllarda belirgin bir şekilde multidisipliner alan olarak öne çıkmıştır. Bu bağlamda, geçiş metali kompleksleri, eşsiz fotokimyasal ve fotofiziksel özelliklerinden ötürü verimli fotosensitizerler olarak kullanılmaktadır. Rutenyum kompleksleri, boyaya duyarlı fotoelektrokimyasal hücrelerde hem fotoduyarlaştırıcılar hem de su oksidasyon katalizörleri olarak çoğunlukla tercih edilmektedir. Fakat onların zehirli ve kıymetli oluşları onların esas dezavantajları olmuştur. Şimdilerde hemen hemen çoğu araştırma alternatiflerini araştırmaya yöneldi. Dünyada bolca bulunan ve kimyasal açıdan kararlı olan altı ligandlı demir kompleksleri (Fe(II)L_6) birçok araştırmacının bu konuda ilgisini çekmektedir. Maalesef, demir-komplekslerinin metalden liganda yük transferi enerjide daha düşük yatan metal merkezli durumlara ultra hızlı deaktivasyon süreci yaşar ve TiO_2 'ye elektron enjeksiyonu için elverişsiz hale gelir. Esas yaklaşım, güçlü alan ligandlarını demir-merkezi ile ilişkilendirerek bu metal merkezli durumlarını istikrarsızlaştırmaktadır. Siyanür ligandının güçlü sigma verme kabiliyetine rağmen, daha önceki çalışmalarda siyanoron polipiridil komplekslerinin duyarlılık performansı araştırılmış ve uyarılmış haldeki süresi arzu edilenden çok daha düşük olduğu gösterilmiştir.

Bu çalışma, donör demir kompleksine sadece elektron veren siyanür gruplarında değil, ayrıca siyanür ligandlarının azot atomlarına koordine edilen kobalt iyonlarında da yardımcı olarak bu sorunu çözmeyi amaçlıyor. Bu amaçla, farklı polipiridil gruplarına ve farklı sayıda siyanür grubuna sahip bir dizi siyanodemir polipiridil kompleksleri hazırlanmıştır. Bu kompleksler, ultraviyole görünür spektroskopisi, Fourier dönüşümlü kızılötesi spektroskopisi, X-ışını fotoelektron spektroskopisi, taramalı elektron mikroskobu ve enerji dağıtıcı X-ışını spektroskopisi

gibi birçok teknikle karakterize edildi.

Bu tezin temeli esas olarak boyaya duyarlı su oksidasyon foto-anodlarının geliştirilmesi üzerine kurulmuştur. Bu çalışmada, su oksidasyon katalitik kobalt bölgeleri koyu lacivert tabakası veren siyanür köprüleme (bridging) grubu yoluyla demir kromoforlarına bağlanmıştır. Siyanür ligandlarının yük aktarma hızı üzerindeki etkisi de araştırılmıştır. Siyanür ligandlarının ve kobalt katalizörünün etkisi hakkında araştırma yapmak için çeşitli malzeme karakterizasyonları yapılmıştır.

Boyaya duyarlılaştırılmış dört farklı fotoanodları üzerine yapılan fotoelektrokimyasal çalışmalar, hem polipiridil ligand tipinin hem de siyanür grup sayısının demir fotosensitizörünün verimliliği üzerinde kritik bir rol oynadığını ortaya koymaktadır. Bu çalışmanın sonuçları, siyanoron polipiridil komplekslerini içeren koyu lacivert analoglarının, etkili boyaya duyarlı fotoelektrokimyasal hücreleri oluşturmak için umut verici düzenekler olabileceğini öne sürmektedir.

Anahtar sözcükler: Demir bazlı fotosensitizerler, Fotosensitizör-su oksidasyon katalizörü dyad, Su yarma, Prusya mavisi analogları, Fotoelektrokimyasal su oksidasyonu.

Acknowledgement

First and Foremost praise is to ALLAH, the Almighty, the greatest of all, on whom ultimately we depend for sustenance and guidance. I would like to thank Almighty Allah for giving me opportunity, determination and strength to do my research. His continuous grace and mercy was with me throughout my life and ever more during the tenure of my research.

I would like to thank my thesis advisor Ass. Prof. Ferdi Karadaş of the Chemistry Department at Bilkent University. The door to Prof. Karadaş office was always open whenever I ran into a trouble spot or had a question about my research or writing. He consistently allowed this paper to be my own work, but steered me in the right the direction whenever he thought I needed it.

I would also like to thank the experts who were involved in the validation survey for this research project: [Prof. Ömer Dağ, Prof. B rak  lg t, Prof. Aysen Yılmaz, Prof. Yavuz Dede]. Without their passionate participation and input, the validation survey could not have been successfully conducted.

Besides my research activities, I also enjoyed my stay in Bilkent University. I thank my fellow colleagues for playing counterstrike in lab during leisure hours. Thanks for giving me such a joyful time.

Finally, I must express my very profound gratitude to my parents, my siblings (Saima Batool, Zoya Batool, Hammad Ali, Amna Ilyas) for providing me with unfailing support and continuous encouragement throughout my years of study. Also not forgetting my family like friends (Ali Sheraz, Misbah Azeem, Salahuddin Zafar, Sidra Noor, M.Abukkar, Dr. Ruby Phul), for immense support through the process of researching and writing this thesis. This accomplishment would not have been possible without them. Thank you.

Contents

1	Introduction	1
1.1	Water Splitting	1
1.1.1	Chromophores/photosensitizers	2
1.2	Challenges In Developing Iron Chromophores	9
1.3	Strategies In Developing Iron Chromophores	13
1.4	Outline	15
2	Experiments and Instrumentation	22
2.1	Chemicals and Reagents	22
2.2	Synthesis of Chromophores	23
2.2.1	Synthesis of $\text{Fe}(\text{bpy})_2(\text{CN})_2 \cdot x\text{H}_2\text{O}$	23
2.2.2	Synthesis of $\text{Fe}(\text{phen})_2(\text{CN})_2 \cdot x\text{H}_2\text{O}$	24
2.2.3	Synthesis of $\text{K}_4[\text{Fe}(\text{bpy})(\text{CN})_4 \cdot x\text{H}_2\text{O}]$	24
2.2.4	Synthesis of $\text{K}_4[\text{Fe}(\text{phen})(\text{CN})_4 \cdot x\text{H}_2\text{O}]$	24

2.3	Synthesis of Semiconductor (Titania Nanowires)	25
2.4	Synthesis of Powder Co-Fe Prussian Blue Analogues (PBAs)	25
2.5	Fabrication of Photoanodes	26
2.6	Instrumentation	27
2.6.1	Ultraviolet-Visible Spectroscopy	27
2.6.2	Fourier Transform Infrared Spectroscopy	27
2.6.3	X-Ray Photoelectron Spectroscopy	27
2.6.4	Scanning Electron Microscopy and Energy-Dispersive X-Ray Spectroscopy	27
2.6.5	Photoelectrocatalytic Studies	28
3	Results and Discussion	29
3.1	UV-Visible Spectroscopy (UV-Vis)	29
3.2	Fourier Transform Infrared Spectroscopy (ATR-FTIR)	32
3.3	X-Ray Photoelectron Spectroscopy (XPS)	35
3.4	Scanning Electron Microscopy (SEM)	38
3.5	Energy Dispersive X-Ray Analysis (EDX)	38
3.6	Photoelectrochemical Measurements of [Co-Fe@TiO ₂ /FTO] Photoanodes	40
3.6.1	Linear Sweep Voltammetry (LSV)	40
3.6.2	Chronoamperometry	44

3.7	Post-Catalytic Characterization	46
3.7.1	Linear Sweep Voltammetry (LSV)	46
3.7.2	X-Ray Photoelectron Spectroscopy (XPS)	48
3.7.3	Scanning Electron Microscopy (SEM) and Energy Dispersive X-ray Analysis (EDX)	50
3.7.4	Incident Photon to Current Efficiency (IPCE)	52
3.7.5	Band Alignment Interpretation	53
4	Conclusion	56

List of Figures

1.1	Generalized phenomena for electron transfer in water oxidation process.	3
1.2	Structure of $[Fe(btz)_3]^{2+}$ complex having 528 ps 3MLCT lifetime.	4
1.3	Primogenic effect in Fe(II) and Ru(II) chromophores.	10
1.4	Comparison of Fe(II) and Ru(II) chromophores in terms of stability of excited states.	11
1.5	Tanabe Sugano Diagram for d^6 configuration.	12
1.6	Effect of CN^- ligand on MC energy levels.	14
1.7	Structures of Iron Chromophores (a) $[FeB_2C_2]$, (b) $[FeP_2C_2]$, (c) $[FeBC_4]$, (d) $[FePC_4]$	15
1.8	Structure of typical Prussian blue, metal ions: red/yellow, N: blue, C: black, interstitial sites: purple.	16
1.9	Structure of Pentacyanoferrate-Coordinated Poly(4-vinylpyridine) PBA.	17
1.10	Fe-CN-Co coordination as a fastest electron relay.	18

1.11	Photoanode Donor-Acceptor system, SC is Semiconductor, ligand is either phenanthroline or bipyridine.	19
1.12	Chronology showing the studies on cyanoiron polypyridyl complexes over past decade.	21
2.1	Synthetic method for $[\text{FeB}_2\text{C}_2]$	23
2.2	Synthetic method for $[\text{FeBC}_4]$	24
2.3	Synthesis of Titania nanowire arrays.	25
2.4	In situ formation of Prussian blue film over Titania surface.	26
3.1	UV-Vis absorption profiles of (a) $[\text{FeB}_2\text{C}_2]$, $[\text{FeBC}_4]$, (b) $[\text{FeP}_2\text{C}_2]$, $[\text{FePC}_4]$ in a wavelength range 280nm-700nm, (c) MLCT bands of $[\text{FeB}_2\text{C}_2]$, $[\text{FeBC}_4]$, (d) MLCT bands of $[\text{FeP}_2\text{C}_2]$, $[\text{FePC}_4]$	30
3.2	UV-Vis absorption profiles (MLCT bands) of (a) $[\text{Co-FeB}_2\text{C}_2]$, (b) $[\text{Co-FeP}_2\text{C}_2]$, (c) $[\text{Co-FeBC}_4]$, (d) $[\text{Co-FePC}_4]$	31
3.3	(a) IR spectra of Iron Chromophores, (b) extended cyanide stretches of Iron Chromophores.	32
3.4	Cyanide stretches of Co-Fe PBAs in IR region (a) $[\text{FeB}_2\text{C}_2\text{Co-}]$, (b) $[\text{Co-FeP}_2\text{C}_2]$, (c) $[\text{Co-FeBC}_4]$, (d) $[\text{Co-FePC}_4]$	34
3.5	N1s and Fe2p XPS spectra of of Fe-complexes and Co-Fe PBAs.	36
3.6	Co2p XPS spectra of of Co-Fe PBAs.	37
3.7	SEM images of (a) $[\text{FeB}_2\text{C}_2]$ (b) $[\text{FeP}_2\text{C}_2]$ (c) $[\text{FeBC}_4]$ (d) $[\text{FePC}_4]$	38
3.8	EDX analysis of (a) $[\text{FeB}_2\text{C}_2]$ (b) $[\text{FeP}_2\text{C}_2]$ (c) $[\text{FeBC}_4]$ (d) $[\text{FePC}_4]$	39

3.9	EDX analysis of (a) [Co-FeB ₂ C ₂] (b) [Co-FeP ₂ C ₂] (c) [Co-FeBC ₄] (d) [Co-FePC ₄].	40
3.10	LSV curves of Bare-TiO ₂ (Red, Closed square=Light, Open square=Dark), [Co-PB@TiO ₂] (Pink, Closed triangle=Light, Open triangle=Dark), [Co-FeBC ₄ @TiO ₂] (Wine, Closed circle=Light, Open circle=Dark) and [Co-FeC ₄ @TiO ₂] (magenta, Closed circle=Light, Open circle=Dark).	42
3.11	LSV curves of Bare-TiO ₂ (Red, Closed square=Light, Open square=Dark), [Co-PB@TiO ₂] (Pink, Closed triangle=Light, Open triangle=Dark), [Co-FeB ₂ C ₂ @TiO ₂] (Blue, Closed circle=Light, Open circle=Dark) and [Co-FeP ₂ C ₂ @TiO ₂] (Brown, Closed circle=Light, Open circle=Dark).	43
3.12	Short-term chronoamperometry (300s, $\nu=50\text{mV/s}$) (a) [Co-FeB ₂ C ₂ @TiO ₂] (blue) (b) [Co-FeP ₂ C ₂ @TiO ₂] (brown) (c) [Co-FeBC ₄ @TiO ₂] (wine) (d) [Co-FePC ₄ @TiO ₂] (magenta).	45
3.13	Long-term chronoamperometry (2hr, $\nu=50\text{ mV/s}$, V=1.22 volts versus RHE) (a) [Co-FeB ₂ C ₂ @TiO ₂] (blue), [Co-FeBC ₄ @TiO ₂] (wine) (b) [Co-FeP ₂ C ₂ @TiO ₂] (brown), [Co-FePC ₄ @TiO ₂] (magenta).	46
3.14	Post-catalytic LSV (0.2-2.0 V versus RHE, $\nu=50\text{ mV/s}$), (a) [Co-FeBC ₄ @TiO ₂], (b) [Co-FePC ₄ @TiO ₂], Red=Before stability test, Black=After stability test.	47
3.15	Post-catalytic LSV (0.2-2 V vs RHE, $\nu=50\text{ mV/s}$), (a) [Co-FeB ₂ C ₂ @TiO ₂], (b) [Co-FeP ₂ C ₂ @TiO ₂], Red=Before stability test, Black=After stability test.	48
3.16	Pristine and Postcatalytic XPS of [Co-FeBC ₄ @TiO ₂], Red=Pristine, Black=Postcatalytic.	49

3.17	Pristine and Postcatalytic XPS of [Co-FePC ₄ @TiO ₂], Red=Pristine, Black=Postcatalytic.	50
3.18	SEM images of (a) [Co-FeBC ₄] PBA pristine, (b) [Co-FeBC ₄] PBA postcatalytic, (c) [Co-FePC ₄] PBA pristine, (d) [Co-FePC ₄] PBA postcatalytic.	51
3.19	EDX analysis of (a) [Co-FeBC ₄ @TiO ₂] postcatalytic, (b) [Co-FePC ₄ @TiO ₂] postcatalytic.	52
3.20	IPCE (%) of (a) [Co-FeB ₂ C ₂ @TiO ₂], [Co-FeP ₂ C ₂ @TiO ₂], (b) [Co-FeBC ₄ @TiO ₂], [Co-FePC ₄ @TiO ₂].	53
3.21	Band diagram for (a) [Co-FeBC ₄ @TiO ₂], (b) [Co-FePC ₄ @TiO ₂], arrows show the movement of charges after illumination.	54
3.22	Band diagram for (a) [Co-FeB ₂ C ₂ @TiO ₂], (b) [Co-FeP ₂ C ₂ @TiO ₂], arrows show the movement of charges after illumination.	55

List of Tables

1.1	Metal-to-ligand charge transfer Lifetimes of Iron-Chromophores Reported so far.	8
2.1	Proposed abbreviations for the chromophores.	23
3.1	UV-Vis absorption bands of Iron Chromophores.	29
3.2	Molar absorptivities of Iron chromophores in UV-Vis region.	30
3.3	UV-Vis absorption profiles of Co-Fe PBAs.	32
3.4	Characteristic IR stretching and bending bands of iron chromophores, (s) is the frequency for stretching mode whereas (b) is the frequency for bending mode.	33
3.5	Comparison of cyanide stretches in Fe-CN (chromophores) and Fe-CN-Co (PBA).	35
3.6	Binding Energies of Fe2p and N1s of Iron Chromophores.	35
3.7	Binding energies of Co2p of Iron Chromophores.	37
3.8	Molecular formulas of Co-Fe PBAs (powder samples) calculated using EDX % atomic ratios.	39

3.9	Comparison of Current Densities obtained by linear sweep voltammetry at Potential of 1.0 V vs RHE.	41
3.10	Difference in current densities ($\mu\text{A}/\text{cm}^2$) of (a) $[\text{Co-FeB}_2\text{C}_2@\text{TiO}_2]$ (blue) and $[\text{Co-FeBC}_4@\text{TiO}_2]$ (wine) (b) $[\text{Co-FeP}_2\text{C}_2@\text{TiO}_2]$ (brown) and $[\text{Co-FePC}_4@\text{TiO}_2]$ (magenta) before and after 2hr chronoamperometry.	45
3.11	Binding Energies of Co2p of pristine and postcatalytic electrodes.	49
3.12	Binding Energies of N1s of pristine and postcatalytic electrodes. .	49
3.13	Binding Energies of Fe2p of pristine and postcatalytic electrodes.	50
3.14	Molecular formulas of $[\text{Co-Fe}/\text{TiO}_2]$ (post-catalytic) calculated using EDX % atomic ratios.	52

Abbreviations

ν	Scan rate
μ	Micro
A	Ampere
V	Volts
eV	Electron Volts
ps	Picosecond
fs	Femtosecond
j	Current density
λ	Wavelength
Δ_o	Octahedral splitting energy
h	Hour
min	Minutes
RT	Room temperature
RHE	Reference hydrogen electrode
FTO	Fluorine-doped Tin Oxide
HOMO	Highest occupied molecular orbital
LUMO	Lowest unoccupied molecular orbital
MLCT	Metal-to-ligand charge transfer
LMCT	Ligand-to-metal charge transfer
MC	Metal centered
GS	Ground state
ES	Excited state
IET	Interfacial electron transfer
RDF	Radial distribution function

PB	Prussian blue
PBA	Prussian blue analogue
WOC	Water oxidation catalyst
PS	Photosensitizer
SC	Semiconductor
NHC	N-heterocyclic
bpy	2,2'-bipyridine
phen	1,10-phenanthroline
btz	3,3-dimethyl-1,1-bis(p-tolyl)-4,4-bis(1,2,3-triazol-5-ylidene)
tpy	2,2';6',2''-terpyridine
UV-Vis	UV-Visible Spectroscopy
ATR-FTIR	Attenuated Total Reflection-Fourier Transform Infrared Spectroscopy
EDX	Energy Dispersive X-Ray Spectroscopy
XPS	X-Ray Photoelectron Spectroscopy
LSV	Linear Sweep Voltammetry
IPCE	Incident Photon-to-Current Efficiency

Chapter 1

Introduction

Fossil fuels have been considered as the utmost and vital energy source for many years. It is depleting to a great extent and contributes towards global warming we encounter in the present times. As a result, replacing it with a renewable and environment friendly source has been a debatable issue for the past few decades.

Hydrogen is found to be the clean and sustainable energy carrier against fossil fuels [1] [2]. It is captivated in water, biomass, hydrocarbons, alcohols, and other renewable sources i.e. wind energy, solar energy, hydro power, etc. [3] [4] [5]. It can be extracted from these sources. Amongst them, solar energy is the auspicious and favorable source. Sunlight driven water splitting, for acquiring chemical energy in the form of hydrogen fuel, has grabbed much attention in recent years [6] [7].

1.1 Water Splitting

Scientists are zealous towards investigating photoelectrochemical water splitting as the efficient and economical way of converting solar energy to chemical energy as hydrogen fuel [8] [9]. In this context, different strategies have been proposed

which include semiconductor particle systems, semiconductor liquid junction systems, sensitized semiconductor systems, electrocatalysts attached to molecular donor-acceptor systems, photovoltaic cells etc. [8] [10].

From past few decades, photovoltaic cells are considered to be the leading devices for water splitting process [11]. Splitting water directly by means of photocatalysis, has offered many challenges; organizing molecular species into suitable sequence leading to charge separation for a longer period of time and choosing suitable catalysts for this reaction (this is the case particularly for four-electron oxidation reaction which is much slower) [10].

The major constituents of artificial photosynthetic systems are; wide band gap semiconductor, photosensitizers and photocatalysts. Many such systems have been devised. Overall, water splitting phenomena for such systems works on the principle that photosensitizer gets photoexcited by absorbing light, leaving holes in ground state, these holes are responsible for oxidizing water to oxygen through water oxidation catalyst as shown in Figure 1.1. The electrons in LUMO (lowest unoccupied molecular orbitals) of photosensitizer are transferred to conduction band of semiconductor and move to photocathode carrying out water reduction process [12] [13].

Owing to the fact that oxidation of water is more complicated task than reduction so for now we are only interested in discussing this process. In water oxidation photoanodes, chromophores are the most crucial elements as they are responsible for sensitizing wide band gap semiconductors for promoting visible light driven water splitting efficiently [14] [15].

1.1.1 Chromophores/photosensitizers

The key requirements for ideal chromophores are as follows;

1. It should absorb in visible region of solar spectrum.

2. It should be abundant.
3. It should be non-toxic and stable.
4. The LUMO level of the chromophore ought to have more negative potential than the conduction band edge of the semiconductor and its HOMO (highest occupied molecular orbital) level should be higher than the LUMO of water oxidation catalyst in order to facilitate the water oxidation reaction efficiently [13].

Based on coordination compounds, only ruthenium complexes have been investigated as the incomparable chromophores so far [16] [17] [18] [13].

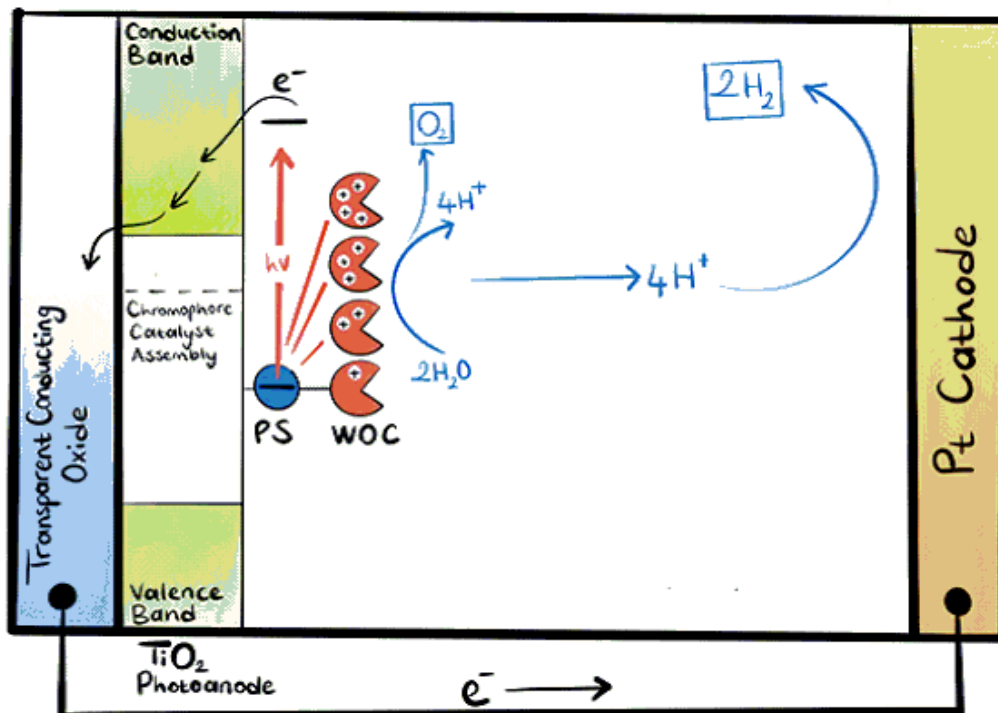


Figure 1.1: Generalized phenomena for electron transfer in water oxidation process.

[19]

Ruthenium based coordination compounds are dominant as chromophores

since they have metal to ligand charge transfer (MLCT) excited states with longer life times and their reduction potentials can be tuned easily. On the other hand, they present certain disadvantages such as being less abundant, highly expensive and toxic [20].

Many iron based chromophores have also been investigated and reported in literature since it is abundant element and it is in the same group as ruthenium. Among them, most of the studies have been performed on N-heterocyclic iron complexes. The simplest $[Fe(bpy)_3]^{2+}$ complex has a lifetime of 0.12 ps, not long enough to carry out photoredox water splitting [21]. 20 ps MLCT lifetime is achieved with $[Fe(bpy)(CN)_4]^{2-}$ complex as photosensitizer without WOC (water oxidation catalyst) [22]. Many computational studies were carried out in past on cyanoiron polypyridine complexes by Jakubikova *et al.* [23] [20]. They have also investigated the effect of linker groups attached to the polypyridyl rings in such systems on the interfacial electron transfer rates (IET). They used five different linker groups attached to polypyridine rings and found that carboxylic acid and phosphonic acid linkers increased the efficiency of interfacial electron transfer (IET) [24]. The rest of the studies are based on cyclometallated and NHC-based iron systems [25] [26] [27]. Among them, the highest MLCT lifetime achieved so far is 528 ps for the complex mentioned in Figure 1.2 [28].

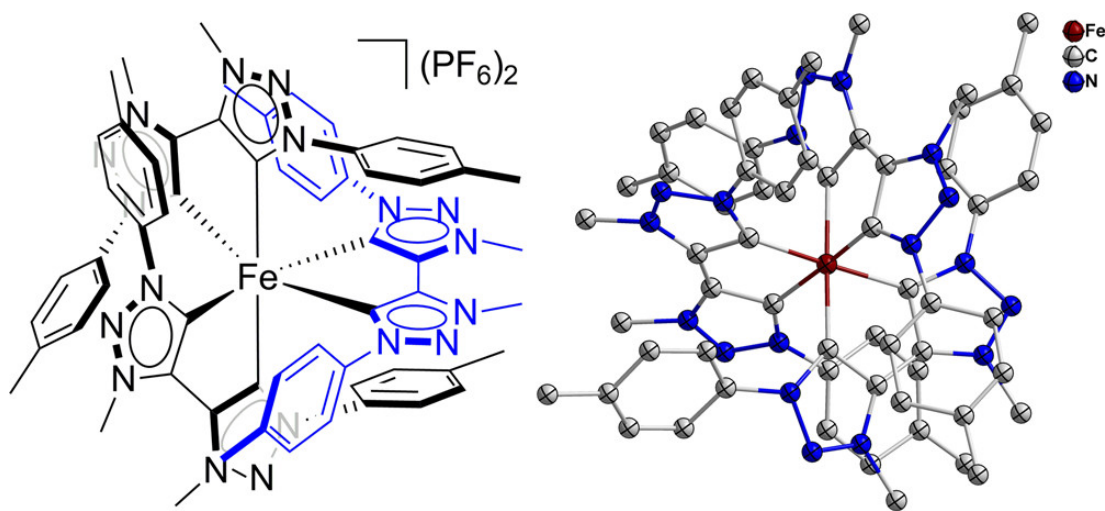
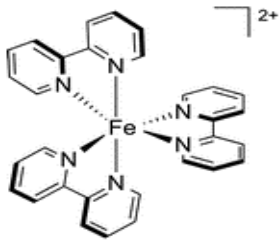


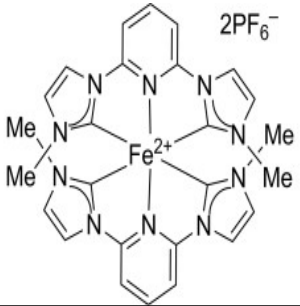
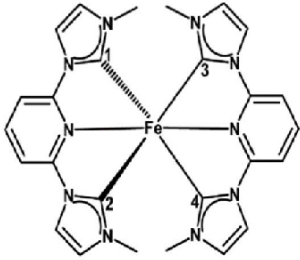
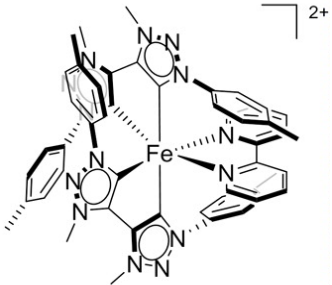
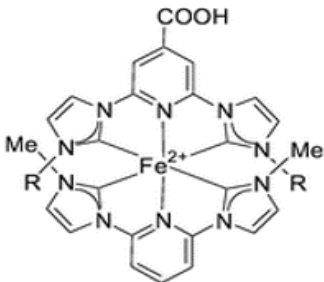
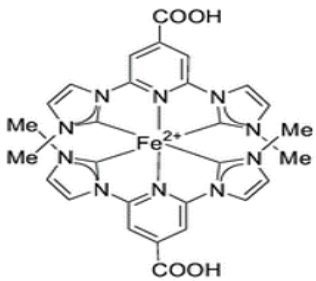
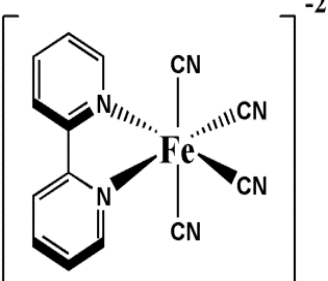



Figure 1.2: Structure of $[Fe(btz)_3]^{2+}$ complex having 528 ps 3MLCT lifetime. [28]

In Table 1.1, MLCT (metal-to-ligand charge transfer) lifetimes of the NHC-Fe complexes reported to date have been listed. These NHC-based iron complexes require tedious and complex organic synthesis which makes them less favourable to be used as potential photosensitizers in devices.

Fe-Chromophores	MLCT-Lifetime	References
	0.12 ps	[21]
	0.15 ps	[21]
	9 ps	[21]

Fe-Chromophores	MLCT-Lifetime	References
	9 ps	[27]
	9 ps	[29]
	13 ps	[30]
	14 ps	[31]

Fe-Chromophores	MLCT-Lifetime	References
	16 ps	[32]
[Fe(dctpy) ₂](BF ₄) ₂]	16 ps	[33]
	19 ps	[34]
	26 ps	[35]

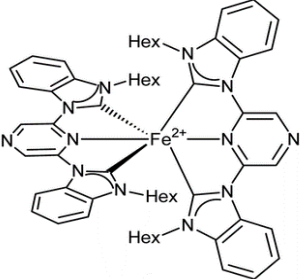
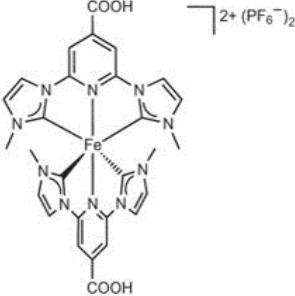
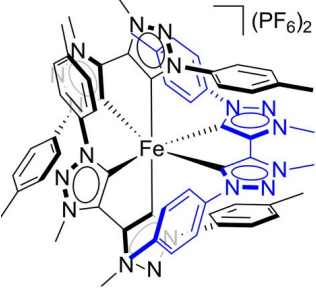
Fe-Chromophores	MLCT-Lifetime	References
	32 ps	[36]
	37 ps	[37]
	528 ps	[28]

Table 1.1: Metal-to-ligand charge transfer Lifetimes of Iron-Chromophores Reported so far.

Table 1.1 explicitly demonstrated the attempts made by various research groups for the vital improvements in MLCT lifetimes exhibited by NHC-based iron complexes, where the lifetime increases down the table. $[\text{Fe}(\text{bpy})_3]^{2+}$ and $[\text{Fe}(\text{tpy})_2]^{2+}$ are not suitable for photochemical applications. So, the substitution of $[\text{Fe}(\text{tpy})_2]^{2+}$ by N-tert-butyl and N-methyl groups increased the ligand field strength which led to significant enhancement of MLCT lifetime. Since, NHC-based complexes have poor π -accepting ability so heteroleptic iron complexes were being synthesized to stabilize MLCT states. The addition of carboxyl groups to these heteroleptic ligands further added to increase the MLCT lifetime. The numbers of NHC and pyridyl ligands and their arrangement around the metal center emerged many iron-chromophores with improved MLCT lifetime. Such an iron chromophore ($[\text{Fe}(\text{btz})_3]^{2+}$, low spin) designed by Warnmark *et al.*, owing to its remarkable ligand field strength presented highest MLCT lifetime till date.

1.2 Challenges In Developing Iron Chromophores

Although Fe is highly abundant, Fe(II)-L₆ complexes have low splitting energy between e_g and t_{2g} compared to their Ru(II) counterparts. This results from weaker interaction of iron with the surrounding ligands leading to low octahedral splitting. This is best explained by primogenic effect, which states that 3s and 3p orbitals of Fe(II) overlaps with its 3d orbitals provoking weaker interaction with the ligand orbitals (Figure 1.3). In contrary, 4d orbitals of Ru(II) can interact strongly with the ligand orbitals since they have lower overlap with 4s and 4d orbitals.

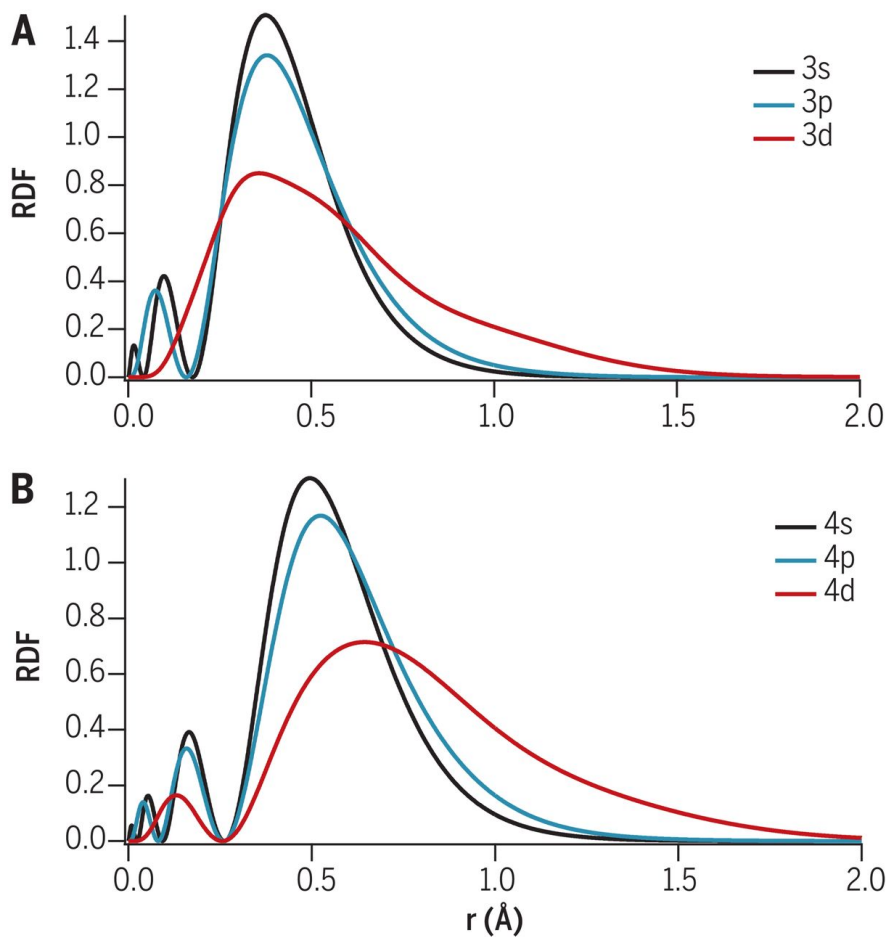


Figure 1.3: Primogenic effect in Fe(II) and Ru(II) chromophores.
[38]

Thus, it has low lying metal centered (eg) states compared to metal-to-ligand charge transfer state (MLCT) as shown in Figure 1.4. As a result, after excitation 3MLCT state is deactivated by this metal centered states in the order of $< 100fs$ making it less feasible for photoelectrochemical applications [38].

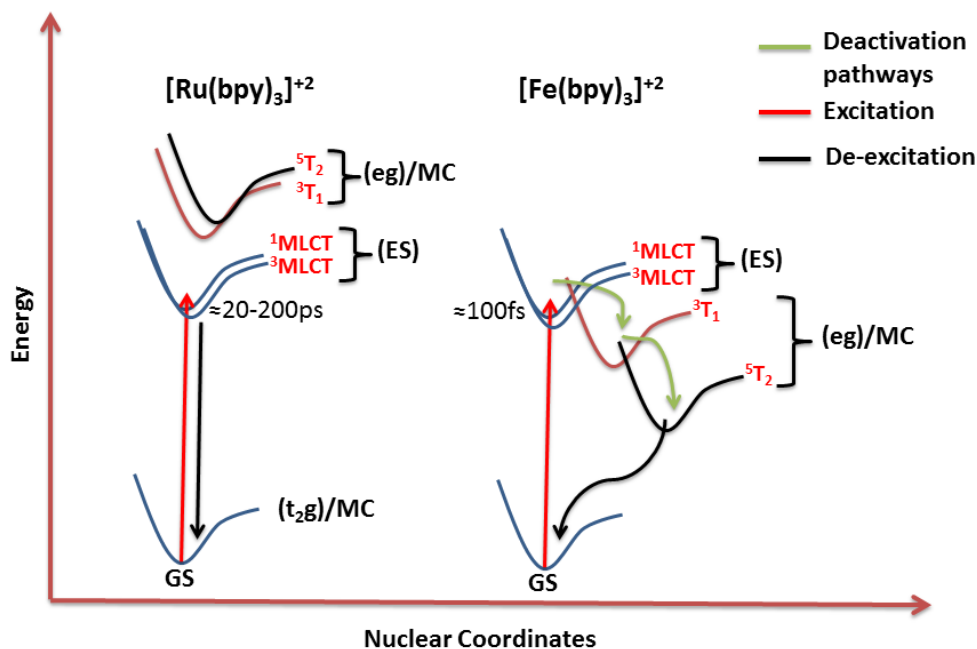


Figure 1.4: Comparison of Fe(II) and Ru(II) chromophores in terms of stability of excited states.

Tanabe Sugano diagram (Figure 1.5) can summarize the repercussions of the primogenic effect as it is related to energy conversion process [38]. The line of intersection separates weak field and high field region showing that splitting energy (Δ_o) is equal to spin pairing energy (P). The ligand field states (term symbols) derived from Russell-Saunders's coupling scheme for d^6 electron configuration are oriented along energy axis. This diagram shows that both Fe(II) and Ru(II) chromophores lie on the high field region and therefore are low spin compounds [38]. However, due to weaker interaction with the ligand orbital MC states (3T_1 , 5T_2) of Fe(II) lie lower in energy than MLCT states (represented by red line in Figure 1.5). This is not the case for Ru(II) chromophores which lead to longer MLCT lifetimes. Many research groups have made attempts to overcome this challenge in case of Fe(II) chromophores [20] [23] [39].

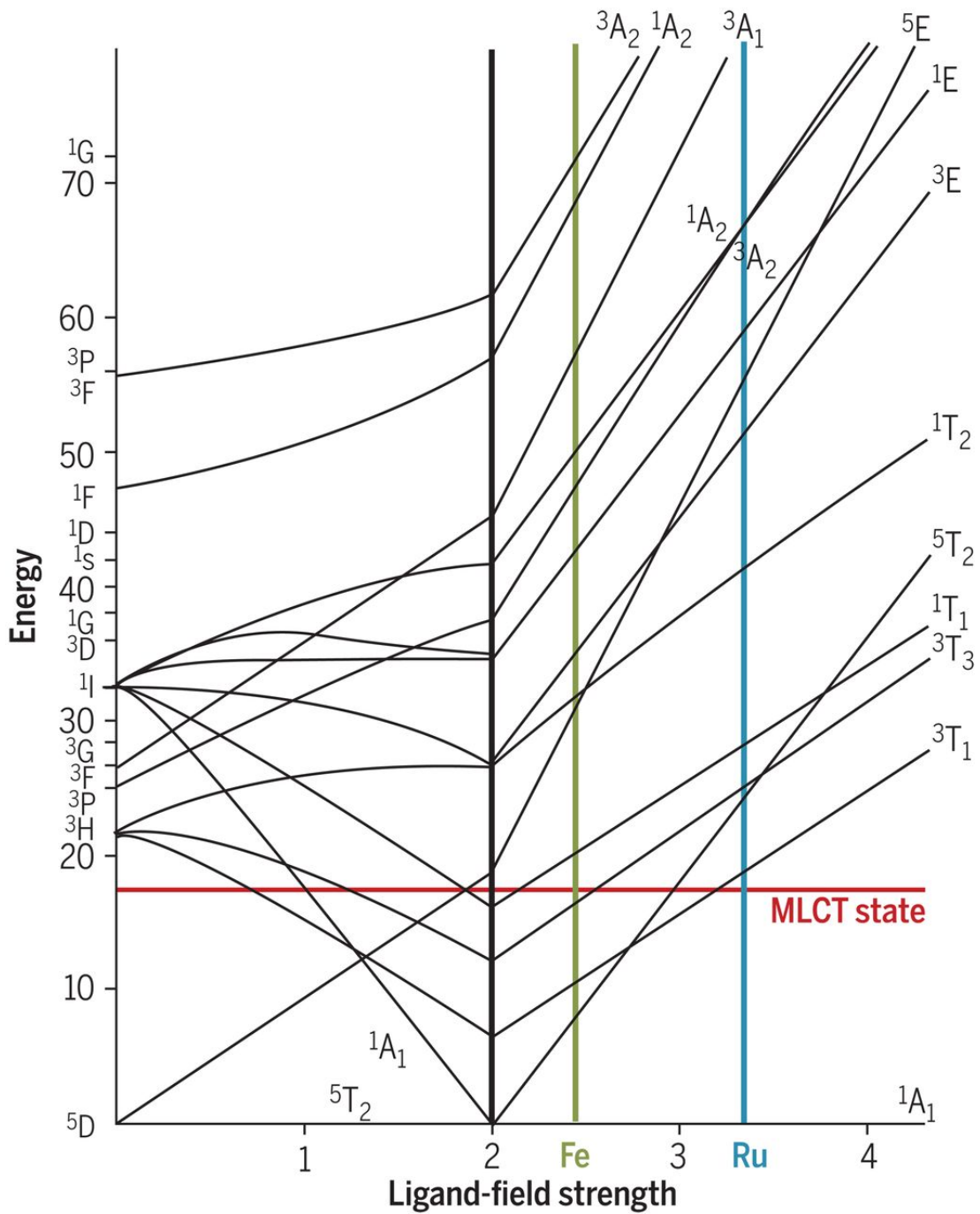


Figure 1.5: Tanabe Sugano Diagram for d^6 configuration.

[38]

1.3 Strategies In Developing Iron Chromophores

Yizhu Liu *et al.* have described that by attaching electron-donating group to the metal, the eg (metal centered, MC) state can be destabilized. Hence, this will stabilize MLCT state compared to metal centered states, making it more accessible energetically. They have used N-heterocyclic carbene complexes for this purpose [21]. The destabilization of MC states has been accomplished so far by the use of cyclometalated Fe(II) complexes [25], N-heterocyclic complexes [40] [21], heteroleptic pyridyl-carbene iron complexes [41], and homoleptic NHC based iron complexes [42]. A review presented by Oliver S. Wenger outlined key challenges and possible strategies employed so far to amplify the photochemical and photophysical properties belong to iron complexes [43]. Some of the strategies mentioned include the use of high symmetry providing ligands (dcpp [44], ddpp [45]), the use of strong σ -donating ligands to destabilize the eg of metal center (NHC-ligands), connecting σ and π -donating ligands with metal center to stabilize MLCT states (cyclometalated ligands [25] [46] [47]), oxidizing Fe^{2+} to Fe^{3+} in order to utilize LMCT (spin allowed) state for sensitization instead of MLCT which is spin forbidden state [48], the use of isoelectronic Cr(0) and Mo(0) complexes for sensitization through MLCT states [49] [50]. Unfortunately, these complexes are difficult to synthesize and are less stable.

In our case, we aimed to use cyano Fe(II) polypyridine (bipyridine and phenanthroline) complexes for the following reasons:

1. They are stable as well as much easier to synthesize.
2. In our chromophores, cyanide ligand, which is a strong σ -donor, is attached to iron center. The σ -donating ability of CN^- ligand will stabilize the eg of metal and its π -accepting ability will raise t_{2g} higher in energy (Figure 1.6). Therefore, this causes increase in energy difference rendering this complex more favorable to be used as chromophore by creating more stabilized $^3\text{MLCT}$ state relative to MC states [38].

3. Additional factor that counts is to increase rate of interfacial electron transfer (IET) from MLCT state to conduction band (CB) of semiconductor. This can be accomplished by attaching suitable linker groups [39] [20] [23] to the ligand (polypyridine) which contributes to two major advantages;

- connecting electron withdrawing group will make $^1,^3MLCT$ states more stable energetically.
- much stronger implantation of chromophore onto semiconductor; both of these factor contribute to enhance IET rate [42].

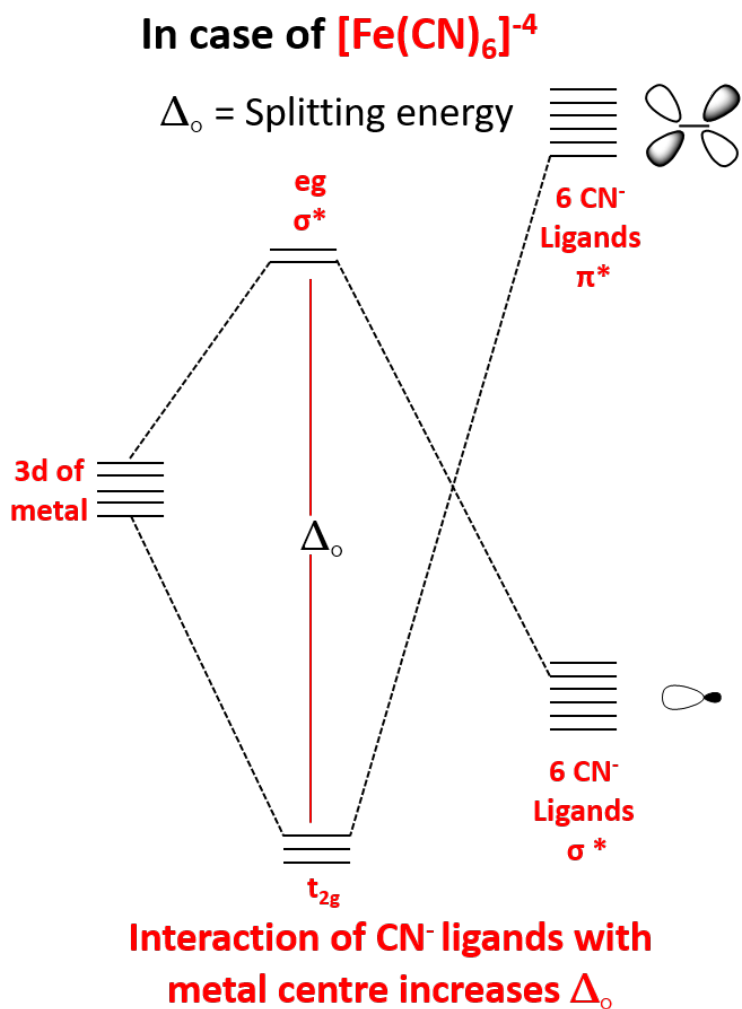


Figure 1.6: Effect of CN^- ligand on MC energy levels.

1.4 Outline

In this thesis, cyanoiron polypyridyl complexes have been synthesized, successfully characterized and tested as chromophores for water splitting application using photoelectrochemical measurements. This study has been done in two parts.

In the first part, Iron chromophores with different number of cyanide ligands as well as polypyridyl rings have been synthesized. The structures of the synthesized chromophores are shown in Figure 1.7. The charge transfer properties and absorption profiles have already been reported in literature which illustrates their potential use as photosensitizers [51] [52] [53] [54].

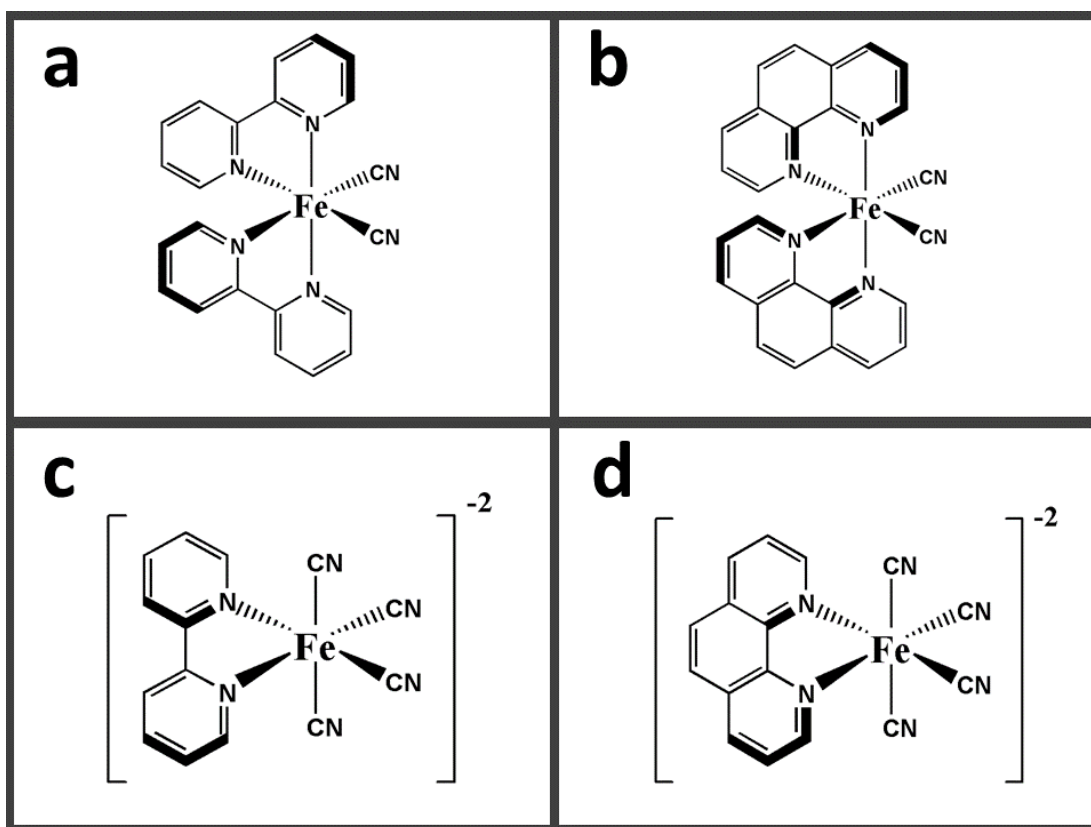


Figure 1.7: Structures of Iron Chromophores (a) [FeB₂C₂], (b) [FeP₂C₂], (c) [FeBC₄], (d) [FePC₄].

However, all these chromophores are not studied or used for photoelectrochemical water splitting before.

Hence in the second part, a novel PS-WOC dyad has been designed and employed for heterogeneous water oxidation photocatalysis. Cobalt-hexacyanometalates could serve as promising catalysts for water oxidation owing to their high catalytic performance as well as stability at pH=7 [55] [56]. Hence, it is linked to Fe-sensitizer emerging non-stoichiometric Prussian blue (PB) network on titania surface for water oxidation.

In a typical Prussian blue structure, hexacyanoiron is connected to cobalt through cyanide ligands and is the prototype of original Prussian blue having combination of metal ions with multiple oxidation states (Figure 1.8).

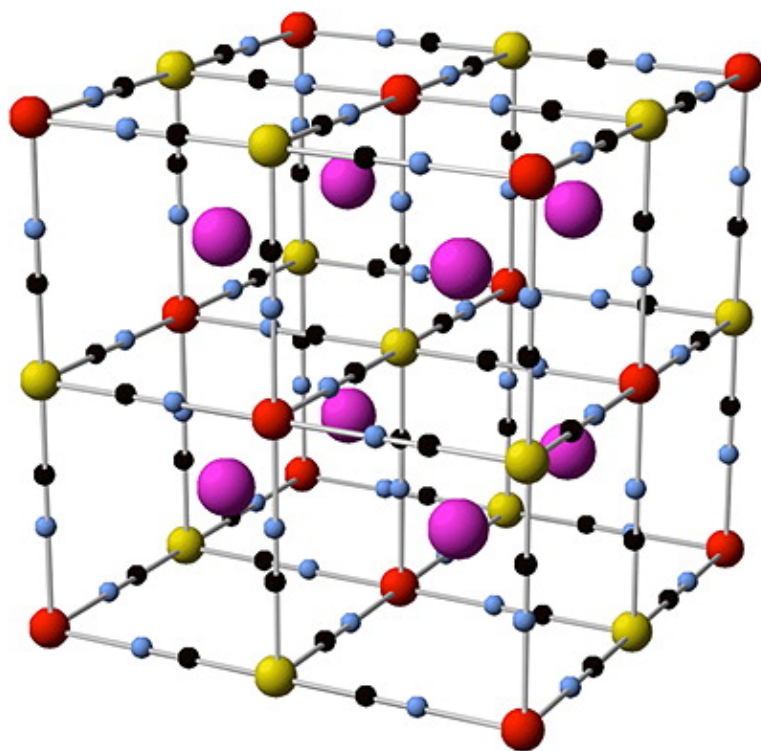


Figure 1.8: Structure of typical Prussian blue, metal ions: red/yellow, N: blue, C: black, interstitial sites: purple.

But it offers a principal disadvantage i.e. low surface concentration of active

water oxidation cobalt sites because of its connection with six cyanide ligands in the structure [57]. Previously reported by our group that reducing the crystallinity of PBA structure by using pentacyanoiron precursor with nitrogen donors (poly(4-vinylpyridine) polymer) can increase the number of cobalt sites (Figure 1.9) [58].

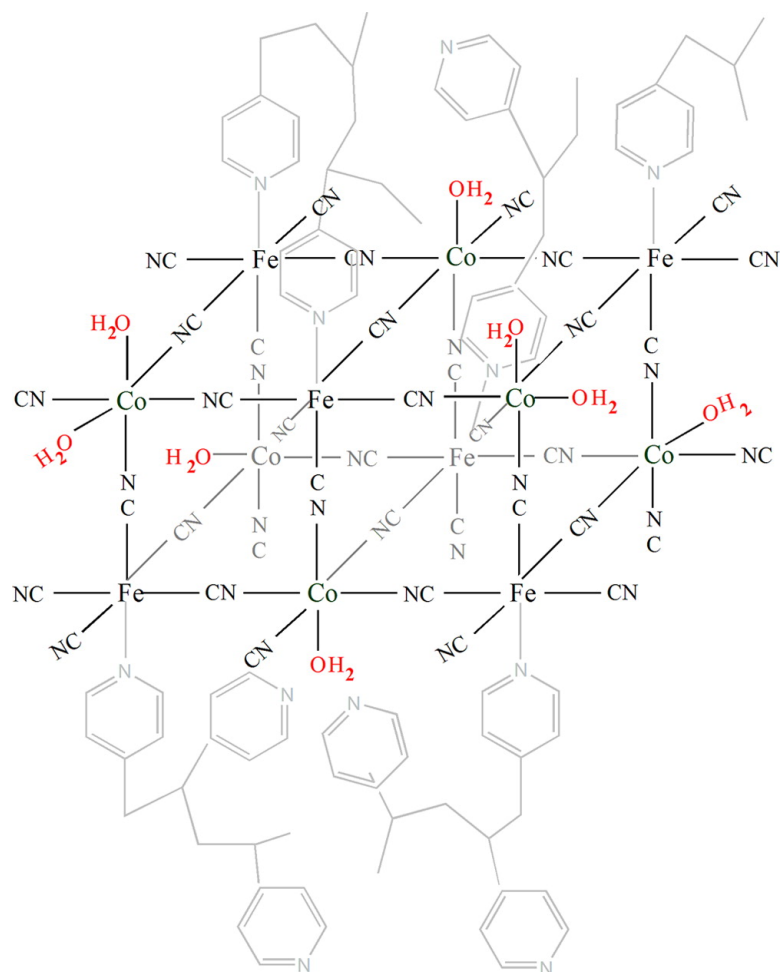


Figure 1.9: Structure of Pentacyanoferrate-Coordinated Poly(4-vinylpyridine) PBA.

These cobalt sites act as a relay for fastest electron transfer to semiconductor through cyanide bridging ligand. Figure 1.10 depicts that these cobalt moieties also serve as σ -donating groups for chromophores [59] [60].

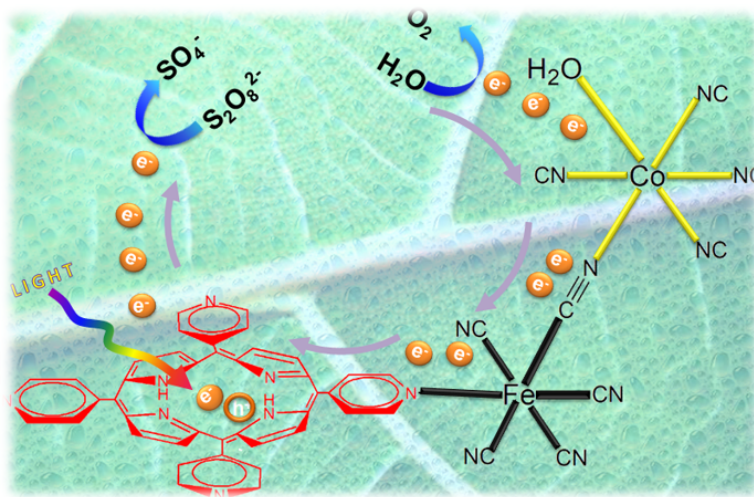


Figure 1.10: Fe-CN-Co coordination as a fastest electron relay.

So we moved one step further to use this strategy and make Prussian blue analogues by reacting our iron chromophores with cobalt, which is a water oxidation catalyst as well as electron donor for iron chromophores. These Prussian blue systems are convenient to synthesize and are highly efficient for water oxidation process [61] [62] [56] [63].

Our photoanode assemblies act as donor-acceptor systems in which each component acts as a donor or acceptor with respect to other upon illumination. Figure 1.11 shows that the process of water oxidation is initiated with the excitation of chromophore leading to MLCT (metal-to-ligand charge transfer) transition. The electron from the LUMO (lowest unoccupied molecular orbital) of chromophore is transferred to the conduction band of titania. The hole in HOMO (highest occupied molecular orbital) of Fe(II) is taken by the cobalt catalyst, which in turn oxidizes water to oxygen.

Each component in the assembly has multiple functions:

1. Co: Water oxidation catalyst (WOC);
 - It connects all the molecular structure together in the form of random non-stoichiometric Prussian-blue (PB) network.

- It increases the sigma donating ability of CN^- by donating e^- .
2. Iron complex: sensitizes the semiconductor (SC).
 3. CN^- :
 - It is responsible for robust coordination.
 - It provides e^- transfer connection between catalyst and photosensitizer (PS).
 - It increases Δ_o (octahedral splitting energy).
 4. TiO_2 : is a semiconductor, which transfers the electrons to photocathode.

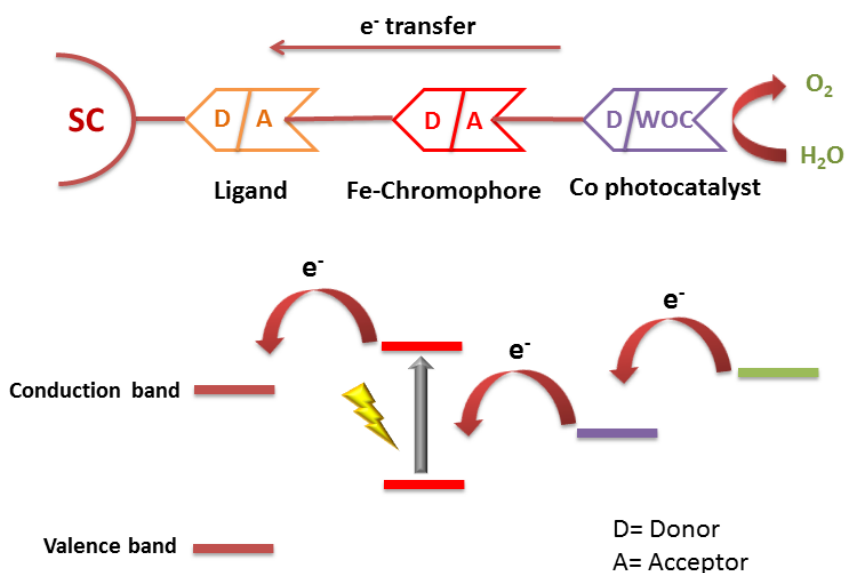


Figure 1.11: Photoanode Donor-Acceptor system, SC is Semiconductor, ligand is either phenanthroline or bipyridine.

Till now, iron chromophores with complex organic ligands have been designed. So it is difficult to connect them to a molecular catalyst in order to complete the

next step for water oxidation. However, our approach here is to use simpler iron complexes as photosensitizer and to associate them with cobalt catalyst overall generating Prussian blue analogue for water oxidation. Unlike other studies, this study utilised Prussian blue analogue which was formed in situ and it is the ideal condition for DSPECs.

Therefore, photoelectrochemical measurements demonstrated that these iron complexes can be utilized as photosensitizers. Furthermore, the effect of cobalt catalyst additionally connected to these chromophores has been inquired by various characterization techniques. Till date, this is the only study using cyanoiron polypyridyl complexes coupled with cobalt catalyst (PBA) for water oxidation catalysis. This briefly demonstrated in the chronology as well (Figure 1.12) that in 60s, cyano iron polypyridyl complexes were synthesized and characterized by UV-Vis absorption spectroscopy and Infrared spectroscopy. In early 80s, these complexes were used for the assessment of their MLCT (metal-to-ligand charge transfer) states. These complexes grabbed much attention at the end of 20th century, when used for the first time to sensitize titania by selectively involving only one MLCT band. From 2000 to 2017, these iron complexes were broadly investigated by experimental and computational chemists to evaluate the MLCT lifetimes as well as to mitigate the deactivation pathways into MC (metal centered) states.

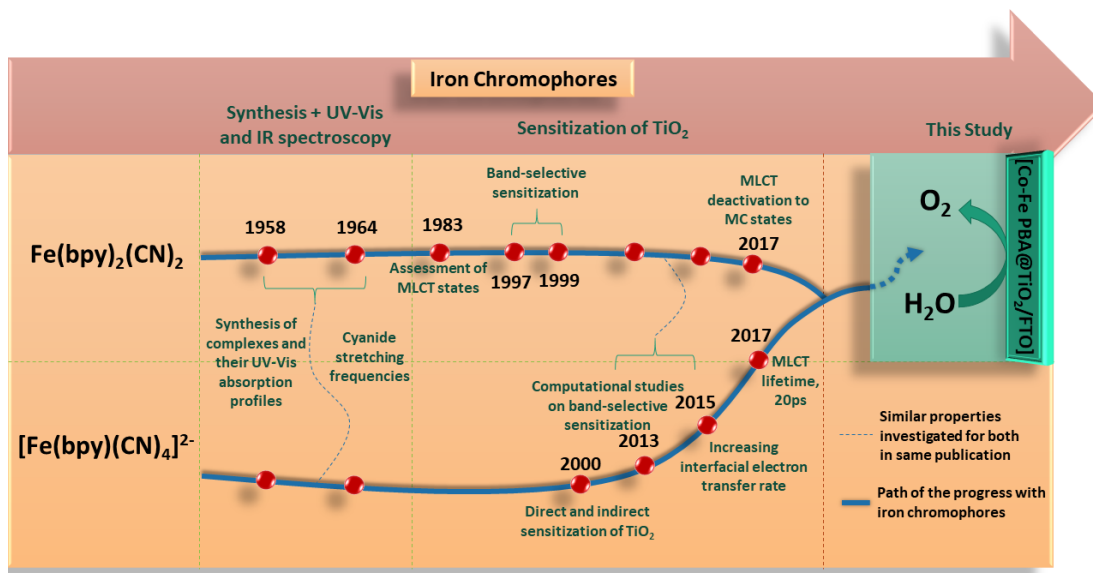


Figure 1.12: Chronology showing the studies on cyanoiron polypyridyl complexes over past decade.

Chapter 2

Experiments and Instrumentation

2.1 Chemicals and Reagents

Iron(II) ammonium sulfate hexahydrate $Fe(SO_4)_2(NH_4)_2 \cdot 6H_2O$ (Carlo Ebra), 2,2'-bipyridine (Acros Organics, 99%), 1,10-phenanthroline (Sigma Aldrich, 99%), Potassium Cyanide KCN (Merck, 65.12 $gmol^{-1}$) were used. For hydrothermal synthesis of Titania (TiO_2) nanowires on FTO coated glass ($7 \Omega sq^{-1}$, Solaronix), Titanium (IV) butoxide ($Ti(OBu)_4$, 97%, Sigma-Aldrich), hydrochloric acid (HCl , 36%, Sigma-Aldrich), Cobalt Nitrate ($Co(NO_3)_2$,), Cobalt Chloride ($CoCl_2$,) and HPLC-grade water (H_2O) were used. Methanol and ethanol solvents were used as such without further purification. Millipore deionized water (resistivity: 18 $m\Omega cm$) was used throughout the experimental procedures.

2.2 Synthesis of Chromophores

Throughout the thesis, abbreviations will be used for the synthesized chromophores as mentioned in the table 2.1;

Complexes	Abbreviations
$\text{Fe}(\text{bpy})_2(\text{CN})_2 \cdot x\text{H}_2\text{O}$	$[\text{FeB}_2\text{C}_2]$
$\text{Fe}(\text{phen})_2(\text{CN})_2 \cdot x\text{H}_2\text{O}$	$[\text{FeP}_2\text{C}_2]$
$\text{K}_2[\text{Fe}(\text{bpy})(\text{CN})_4 \cdot x\text{H}_2\text{O}]$	$[\text{FeBC}_4]$
$\text{K}_2[\text{Fe}(\text{phen})(\text{CN})_4 \cdot x\text{H}_2\text{O}]$	$[\text{FePC}_4]$

Table 2.1: Proposed abbreviations for the chromophores.

2.2.1 Synthesis of $\text{Fe}(\text{bpy})_2(\text{CN})_2 \cdot x\text{H}_2\text{O}$

This complex was synthesized according to literature by a modified procedure [64]. Solution of 2,2'-bipyridine in 10 ml methanol was added slowly and dropwise to 1:3 methanol+water solution of $\text{Fe}(\text{NH}_4)_2(\text{SO}_4)_2 \cdot 6\text{H}_2\text{O}$ at room temperature. The mixture was left for overnight stirring. This solution was filtered and solution of KCN (in 5 ml methanol) was added dropwise to the filtrate. The mixture was again kept overnight for stirring. Methanol was removed from the reaction mixture by rotary evaporator and complex was precipitated leaving it in refrigerator for 24 hours (Figure 2.1). Violet colored precipitates were collected by vacuum suction and washed with small amount of methanol and dried. A yield of about 72% was obtained for the synthesized complex.

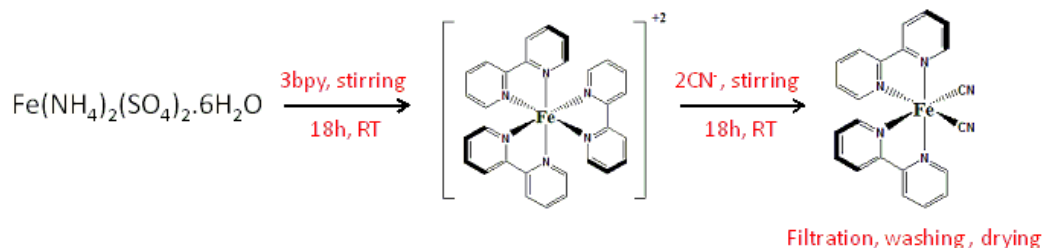


Figure 2.1: Synthetic method for $[\text{FeB}_2\text{C}_2]$.

2.2.2 Synthesis of $\text{Fe}(\text{phen})_2(\text{CN})_2 \cdot x\text{H}_2\text{O}$

Similar procedure was followed for its synthesis as above. Dark red colored precipitates were obtained at the end of experiment (yield= 73%) [64].

2.2.3 Synthesis of $\text{K}_4[\text{Fe}(\text{bpy})(\text{CN})_4] \cdot x\text{H}_2\text{O}$

It was synthesized with slight modification in a method already reported in literature [64]. In a round bottom flask, 100 mg FeB_2C_2 (as synthesized above) and 29 mg KCN in 100ml of water were added. This mixture was refluxed with constant stirring at 90°C for a period of 5 days. Resulting mixture was reduced to half by rotary evaporator and kept in refrigerator in order to precipitate the desired product with a yield of approximately 70% (Figure 2.2). Later, the final product was filtered and its formation was confirmed by UV-Vis spectroscopy.

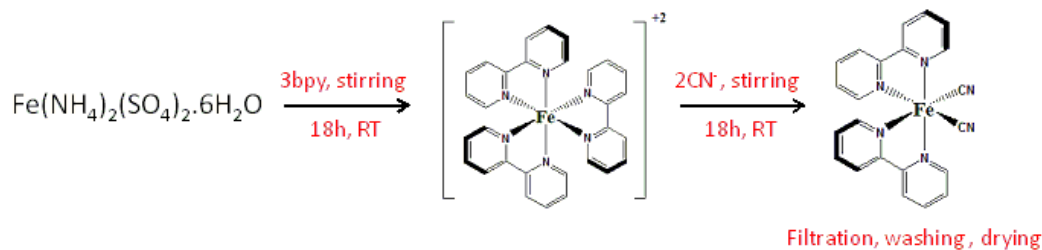


Figure 2.2: Synthetic method for $[\text{FeBC}_4]$.

2.2.4 Synthesis of $\text{K}_4[\text{Fe}(\text{phen})(\text{CN})_4] \cdot x\text{H}_2\text{O}$

It was synthesized following same procedure as above. At the end, the light orange colored product was collected and dried [64]. The product yield obtained was around 75%.

2.3 Synthesis of Semiconductor (Titania Nanowires)

Titania nanowires were grown on thoroughly cleaned FTO glass by hydrothermal process following previously reported procedures [65]. In short, Hydrochloric acid (20 ml) was added in 20 ml of distilled water and allowed to mix for 10min. Afterwards, 1 ml of titanium butoxide was added to the previous solution and kept stirring for 30min. The mixture was poured into 45 ml stainless steel autoclave and FTO is placed at an angle of 45° against the autoclave with its conducting side facing up. It was left in the oven for heating at 180°C for 4h (Figure 2.3). Titania nanowires were grown successfully and rinsed with ethanol solvent. It was then annealed in air at 450°C for about 2 hour and cooled to 150°C [66].

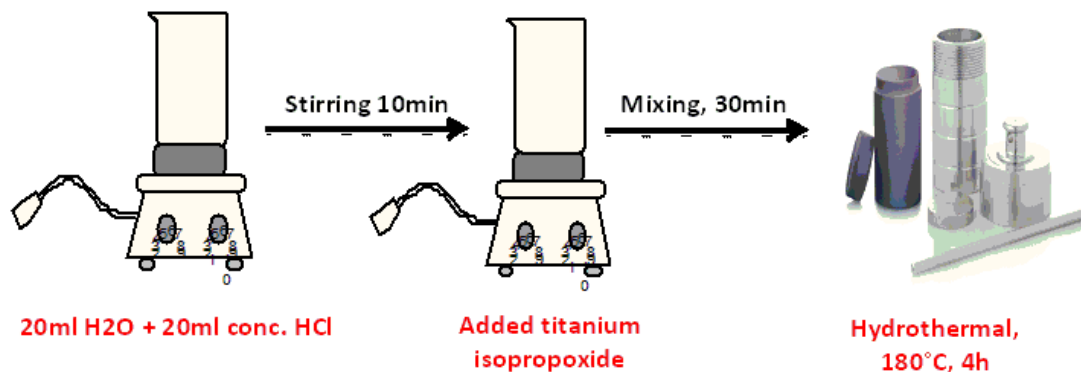


Figure 2.3: Synthesis of Titania nanowire arrays.

2.4 Synthesis of Powder Co-Fe Prussian Blue Analogues (PBAs)

For the synthesis of powder samples of Co-Fe PBAs, both the iron chromophore and cobalt catalyst were dissolved in water. For $[\text{Co-FeB}_2\text{C}_2]$ and $[\text{Co-FeP}_2\text{C}_2]$ synthesis, cobalt chloride (CoCl_2) was used as cobalt source. Cobalt nitrate ($\text{Co}(\text{NO}_3)_2$) was used as cobalt source for $[\text{Co-FeBC}_4]$ and $[\text{Co-FePC}_4]$ synthesis. Both chromophore and cobalt solutions were mixed and stirred continuously for

3 days in case of $[\text{Co-FeB}_2\text{C}_2]$ and $[\text{Co-FeP}_2\text{C}_2]$. After 3 days, the mixture was reduced to half in rotavap and kept in the fridge for 1 day to get precipitates of PBA. In contrast, for $[\text{Co-FeBC}_4]$ and $[\text{Co-FePC}_4]$ synthesis mixing of chromophore and cobalt solution led to immediate precipitation of PBA. At the end, the PBA precipitates were separated from the reaction mixture by the process of centrifugation. The PBA products were dried and characterized. The yield obtained for Co-Fe PBAs was approximately 40%.

2.5 Fabrication of Photoanodes

Titania nanowires were coated with chromophores and catalyst. Chromophores of particular concentration (e.g. 1.33 mM of dye solution in methanol) was prepared and titania coated FTO was immersed into this dye solution for 25min and washed with methanol. After that, it was left in catalyst solution (0.2 M of cobalt nitrate solution in ethanol) for 25min followed by washing with water. This process of dip coating was repeated about four to five times for better dye adsorption. Finally, the Prussian blue film was formed in situ on the titania surface as shown in Figure 2.4. Same procedure was followed for the formation of photoanodes with all the four chromophores.

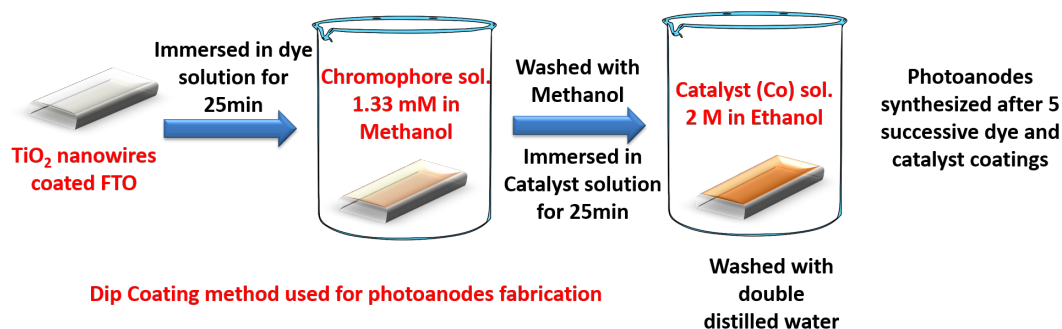


Figure 2.4: In situ formation of Prussian blue film over Titania surface.

2.6 Instrumentation

2.6.1 Ultraviolet-Visible Spectroscopy

The absorption spectra for chromophores were recorded using Carry 5000 UV-Vis-NIR spectrophotometer in a wavelength range of 200-800 nm keeping scan rate 600 nm/min.

2.6.2 Fourier Transform Infrared Spectroscopy

Using Bruker Alpha Platinum-ATR Spectrometer FTIR spectra were recorded in transmission mode within the wavenumber range of 400-4000 cm^{-1} for 64 scans.

2.6.3 X-Ray Photoelectron Spectroscopy

XPS analysis was carried out using Thermo Scientific K-Alpha X-Ray Photoelectron Spectrometer having an $\text{AlK}\alpha$ microfocused monochromator source working at spot size of 400 μm and $h\nu=14.866$ eV accompanied by a flood gun for charge neutralization, 200 eV for survey scan and 10-30 eV for individual scans. All the peaks were shifted with reference to C1s positioned at 284.8 eV.

2.6.4 Scanning Electron Microscopy and Energy-Dispersive X-Ray Spectroscopy

SEM and EDX measurements were recorded using FEI-Quanta 200 FEG ESEM. SEM images were obtained at a beam voltage of 5 kV and Spot size of 3.0. Whereas, for EDX analysis 5.0 spot size and 15 kV beam voltage was maintained.

2.6.5 Photoelectrocatalytic Studies

Photoelectrocatalytic measurements were performed using Gamry Instruments Interface 1000 Potentiostat/Galvanostat at ambient temperature. A conventional three electrode setup consisting of Ag/AgCl (3.5 M KCl) reference electrode, Pt-wire as counter electrode and our photoanodes (Prussian blue coated TiO₂/FtO) as working electrodes. All the measurements were recorded at neutral pH (7) using phosphate buffer (0.1 M using KH₂PO₄ and K₂HPO₄ salts in deionized water). Similar to previous studies, all the electrodes were dipped into the electrolyte (buffer solution) and purged with N₂ for 10 minutes to get rid of dissolved O₂. Electrolyte was changed after each photoanode measurement in order to get correct data. All the measured potential values were referenced with respect to RHE (reference hydrogen electrode) and corrected based on the surface area of working electrode.

Chapter 3

Results and Discussion

3.1 UV-Visible Spectroscopy (UV-Vis)

In the UV-Vis spectra, [FeB₂C₂] and [FeBC₄] complexes exhibit two metal-to-ligand charge transfer bands at 521 nm with band edge at 481 nm, 351 nm and 486 nm, 347 nm respectively. Also, ligand based $\pi - \pi^*$ transition were demonstrated at 297 nm and 295 nm for [FeB₂C₂] and [FeBC₄] respectively (Figure 3.1a).

Complexes	$\pi - \pi^*$ (nm)	MLCT (nm)
[FeB ₂ C ₂]	297	(521,481), 351
[FeP ₂ C ₂]	267	(512,451)
[FeBC ₄]	295	486, 347
[FePC ₄]	265	465

Table 3.1: UV-Vis absorption bands of Iron Chromophores.

Similarly, MLCT bands are observed at 512 nm with shoulder at 451 nm and 465 nm as well as ligand based bands at 267 nm and 265 nm for [FeP₂C₂] and [FePC₄] complexes respectively (Figure 3.1b). The more number of cyanide ligands in [FeBC₄] and [FePC₄] stabilize the t_{2g} of iron center, exhibiting a blue shift. Overall, [FeB₂C₂] and [FeP₂C₂] complexes exhibit slightly higher molar absorptivities calculated using bands at around 500 nm in UV-Vis region than [FeBC₄] and [FePC₄], as shown in Table 3.2. The UV-Vis profiles of all these four

chromophores are in accordance with the literature [64].

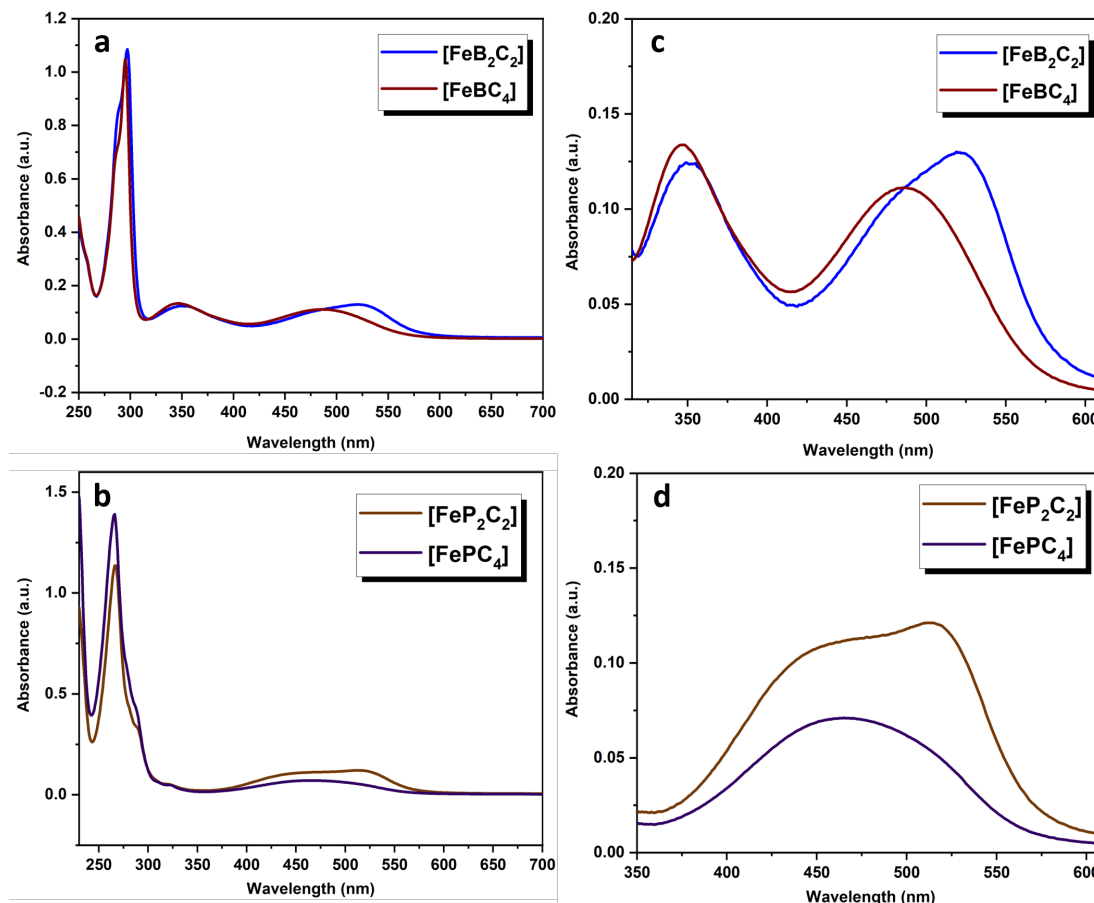


Figure 3.1: UV-Vis absorption profiles of (a) $[\text{FeB}_2\text{C}_2]$, $[\text{FeBC}_4]$, (b) $[\text{FeP}_2\text{C}_2]$, $[\text{FePC}_4]$ in a wavelength range 280nm-700nm, (c) MLCT bands of $[\text{FeB}_2\text{C}_2]$, $[\text{FeBC}_4]$, (d) MLCT bands of $[\text{FeP}_2\text{C}_2]$, $[\text{FePC}_4]$.

Complexes	Molar absorptivity ($\text{L mol}^{-1}\text{cm}^{-1}$)
$[\text{FeB}_2\text{C}_2]$	9.969×10^4
$[\text{FeP}_2\text{C}_2]$	9.751×10^4
$[\text{FeBC}_4]$	7.873×10^4
$[\text{FePC}_4]$	7.403×10^4

Table 3.2: Molar absorptivities of Iron chromophores in UV-Vis region.

The UV-Vis absorption profiles for $[\text{Co-FeBC}_4]$, $[\text{Co-FePC}_4]$, $[\text{Co-FeB}_2\text{C}_2]$ and $[\text{Co-FeP}_2\text{C}_2]$ are also elucidated in Figure 3.2. It shows a red shift in all cases however, this shift is not significant in the case of $[\text{Co-FeB}_2\text{C}_2]$ and $[\text{Co-FeP}_2\text{C}_2]$

PBAs. The profiles of all PBAs are almost similar to the absorption profiles of all chromophores. This can be attributed to the stabilization of MLCT states, or destabilization of ground state or both as a result of coordination of cobalt sites. In case of PBAs having $[\text{FeBC}_4]$ and $[\text{FePC}_4]$ chromophores, the MLCT bands are much broader which correspond to the formation of extended Prussian blue network. Nevertheless, owing to the neutrality of $[\text{FeB}_2\text{C}_2]$ and $[\text{FeP}_2\text{C}_2]$, such chromophores based PBAs form small nuclearity clusters as shown by the non-broadening and slight red shift in the UV-Vis region. The exact wavelength values are presented in Table 3.3.

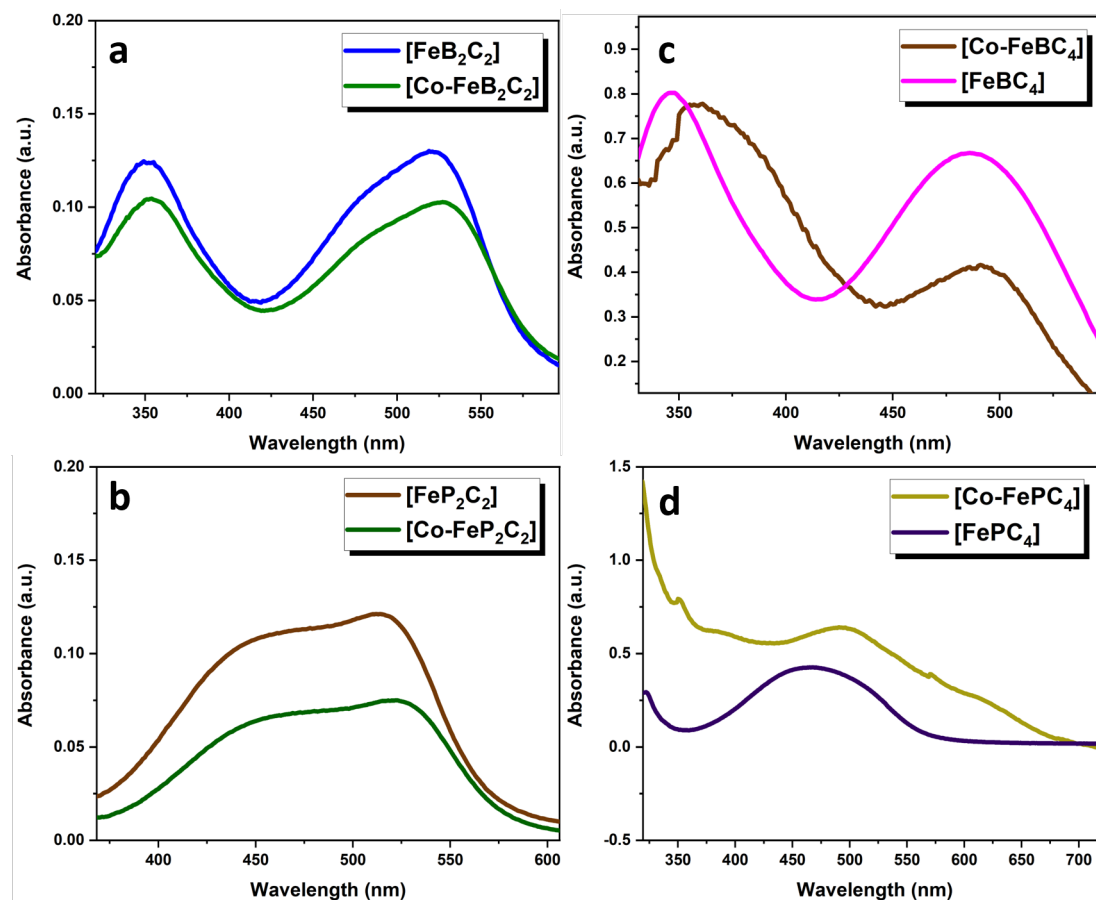


Figure 3.2: UV-Vis absorption profiles (MLCT bands) of (a) $[\text{Co-FeB}_2\text{C}_2]$, (b) $[\text{Co-FeP}_2\text{C}_2]$, (c) $[\text{Co-FeBC}_4]$, (d) $[\text{Co-FePC}_4]$.

Complexes	MLCT (nm)
[Co-FeB ₂ C ₂]	(527,484), 355
[Co-FeP ₂ C ₂]	(524,462)
[Co-FeBC ₄]	495, 360
[Co-FePC ₄]	493

Table 3.3: UV-Vis absorption profiles of Co-Fe PBAs.

3.2 Fourier Transform Infrared Spectroscopy (ATR-FTIR)

In Infrared region, stretches between 2000-2200 cm^{-1} belong to cyanide (CN^{-1}) ligand which attributes to successful attachment of cyanide ligands to iron precursor. The stretches between 500-1600 cm^{-1} demonstrate bipyridine and phenanthroline ligands (Figure 3.3). The characteristic bands are shown in Table 3.4. The four bands in case of [FeBC₄] are attributed to symmetrical and asymmetrical stretching modes of cis and trans cyanide ligands. The fourth band is absent in [FePC₄], which might be due to poor resolution of the instrument. Two CN stretches in [FeP₂C₂] and [FeB₂C₂] are attributed to coupling of stretching motions to symmetrical and asymmetrical modes. This confirms the cis-conformation of [FeP₂C₂] and [FeB₂C₂] complexes [67].

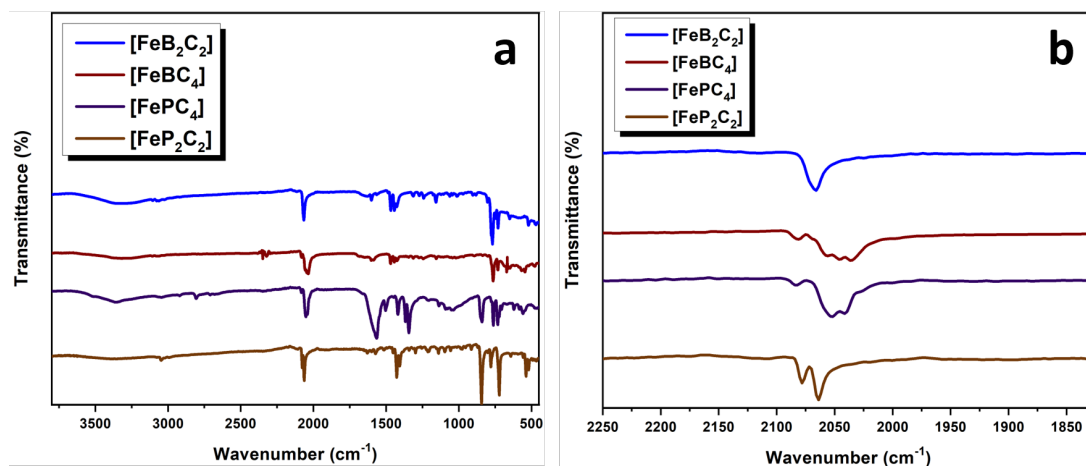


Figure 3.3: (a) IR spectra of Iron Chromophores, (b) extended cyanide stretches of Iron Chromophores.

Complexes	CN ⁻¹ (cm ⁻¹)	H ₂ O (cm ⁻¹)	C-H (cm ⁻¹)	C=C (cm ⁻¹)
[FeB ₂ C ₂]	2066, 2074	1603(b), 3357(s)	767(b), 3077(s)	1470
[FeP ₂ C ₂]	2064,2078	1599(b), 3351(s)	781(b), 3048(s)	1427
[FeBC ₄]	2034, 2044, 2057, 2081	1566(b), 3340(s)	766(b), 3073(s)	1470
[FePC ₄]	2041, 2051, 2084	1572(b), 3338(s)	763(b), 3047(s)	1419

Table 3.4: Characteristic IR stretching and bending bands of iron chromophores, (s) is the frequency for stretching mode whereas (b) is the frequency for bending mode.

These iron complexes were also treated with Co(NO₃)₂ to form Prussian blue analogue and IR analysis was performed on them to see the effect of Co-catalyst on the CN stretch illustrated by Figure 3.4. The CN stretch shifted to higher wavenumber once connected to Co-catalyst given in Table 3.5. This result is comparable to ruthenium-P4VP-CoFe PBA already reported in literature by our group, where a shift to higher cm⁻¹ for CN stretch was observed due to Fe-CN-Co mode of coordination [68]. In case of [FeB₂C₂] and [FeP₂C₂], Fe³⁺ and Co³⁺ bands appear at higher wavenumbers but are very weak to be detectable. Similar trend was observed for [FeBC₄], and [FePC₄] complexes [67]. In contrast, a smaller band at higher wavenumbers (Table 3.5) observed in Co:Fe PBAs suggest the presence of partially oxidized Fe³⁺ sites and Co³⁺ [68].

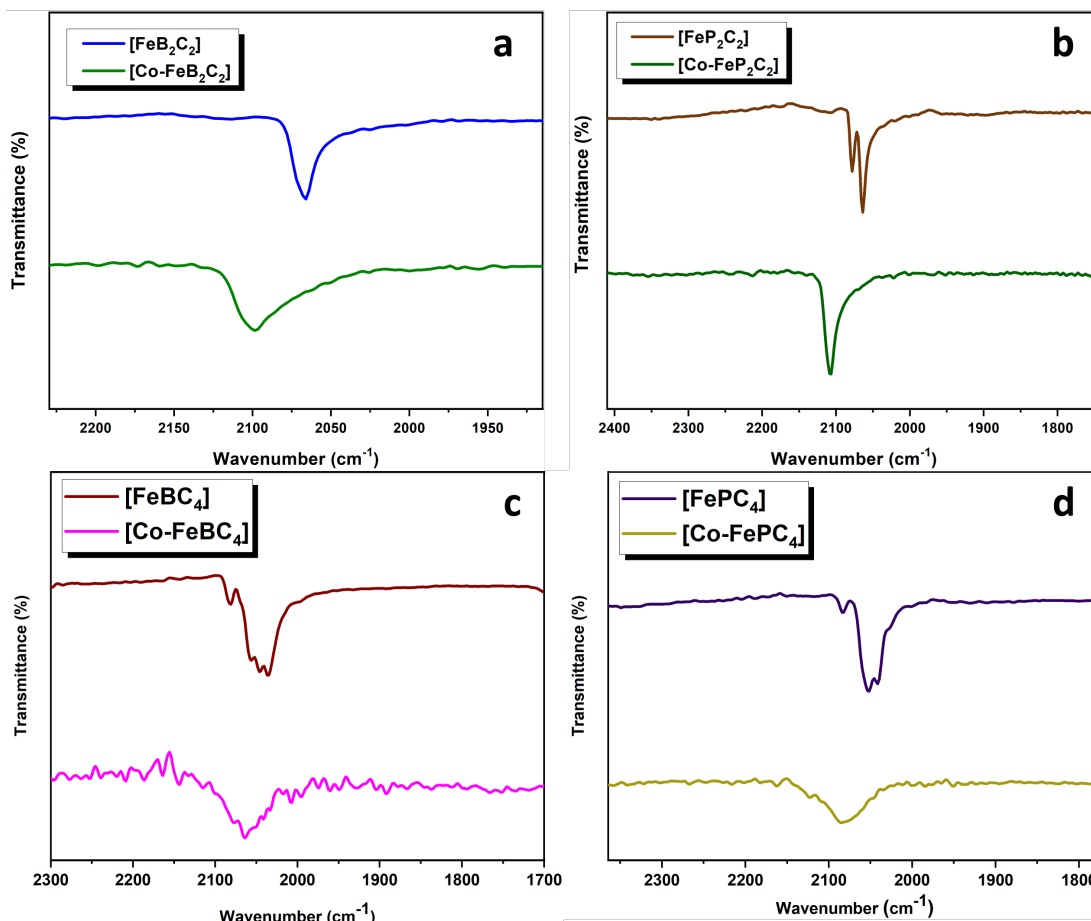


Figure 3.4: Cyanide stretches of Co-Fe PBAs in IR region (a) [FeB₂C₂Co-], (b) [Co-FeP₂C₂], (c) [Co-FeBC₄], (d) [Co-FePC₄].

This depicts that cobalt acts as a donor group toward cyanide and contribute to increase its strength as the addition of Co²⁺ makes the structure even more electron deficient, and therefore it causes an increase in electron donation from σ^* of cyanide and shifts to higher frequency.

A broader cyanide stretch compared to iron precursor is observed due to non-stoichiometric attachment of Co²⁺ ions to iron chromophore as well as oxidation of Fe²⁺ to Fe³⁺ up to a certain extent [68].

Complexes	Fe-CN (cm^{-1})	Fe($^{2+}, ^{3+}$)-CN-Co (cm^{-1})
[FeB ₂ C ₂]	2066, 2074	2099, 2107
[FeP ₂ C ₂]	2064, 2078	2109, 2119
[FeBC ₄]	2034, 2044, 2057, 2081	2064, 2116
[FePC ₄]	2041, 2051, 2084	2086, 2123

Table 3.5: Comparison of cyanide stretches in Fe-CN (chromophores) and Fe-CN-Co (PBA).

3.3 X-Ray Photoelectron Spectroscopy (XPS)

In order to confirm the formation of chromophores XPS spectra were recorded. In Figure 3.5, 2p_{3/2} and 2p_{1/2} of Fe2p exhibit two main peaks at around 708 eV and 720 eV for all the iron complexes [59]. These Fe2p peaks are broad which can be attributed to partial oxidation of Fe²⁺ to Fe³⁺ species (Table 3.6). This is commonly known phenomena in pentacyanoferrate complexes and is in good agreement with IR results showing shoulder band for Fe in 3+ oxidation state [59]. In addition to that, for N1s spectra of all iron complexes, two peaks appeared at around 399 eV and 397 eV. The N1s peak at higher binding energy is due to CN of bipyridine and phenanthroline ligands, and the one at lower binding energy is assigned to CN ligands linked to iron center (Figure 3.5). A slightly higher shift in wavenumber for Co-Fe PBAs is always observed due to association of cobalt with cyanide ligands [59] [68]. Broadening of the features in Co-Fe PBAs indicate the existence of Fe-CN-Co type of coordination mode (Table 3.6).

Complexes	Fe ²⁺ (2p _{1/2} , 2p _{3/2}) (eV)	N1s (eV)
[FeB ₂ C ₂]	720.49, 707.79	397.08, 399.58
[Co-FeB ₂ C ₂]	720.68, 708.08	397.68, 399.58
[FeP ₂ C ₂]	720.78, 708.08	396.58, 399.28
[Co-FeP ₂ C ₂]	721.28, 708.48	397.22, 399.28
[FeBC ₄]	720.78, 708.18	397.18, 399.33
[Co-FeBC ₄]	720.98, 708.28	397.68, 399.58
[FePC ₄]	720.78, 708.08	397.18, 399.28
[Co-FePC ₄]	721.08, 708.28	397.02, 399.48

Table 3.6: Binding Energies of Fe2p and N1s of Iron Chromophores.

As shown in Figure 3.6, Co2p region exhibits two principal bands at ≈ 781

eV and ≈ 797 eV correspond to $2p_{1/2}$ and $2p_{3/2}$ of Co^{2+} for all Co-Fe PBAs. Additional doublet is observed at moderately higher binding energies attributed to Co^{3+} with satellite bands at around ≈ 3 eV higher in eV scale (Table 3.7) [56] [58] [69] [60].

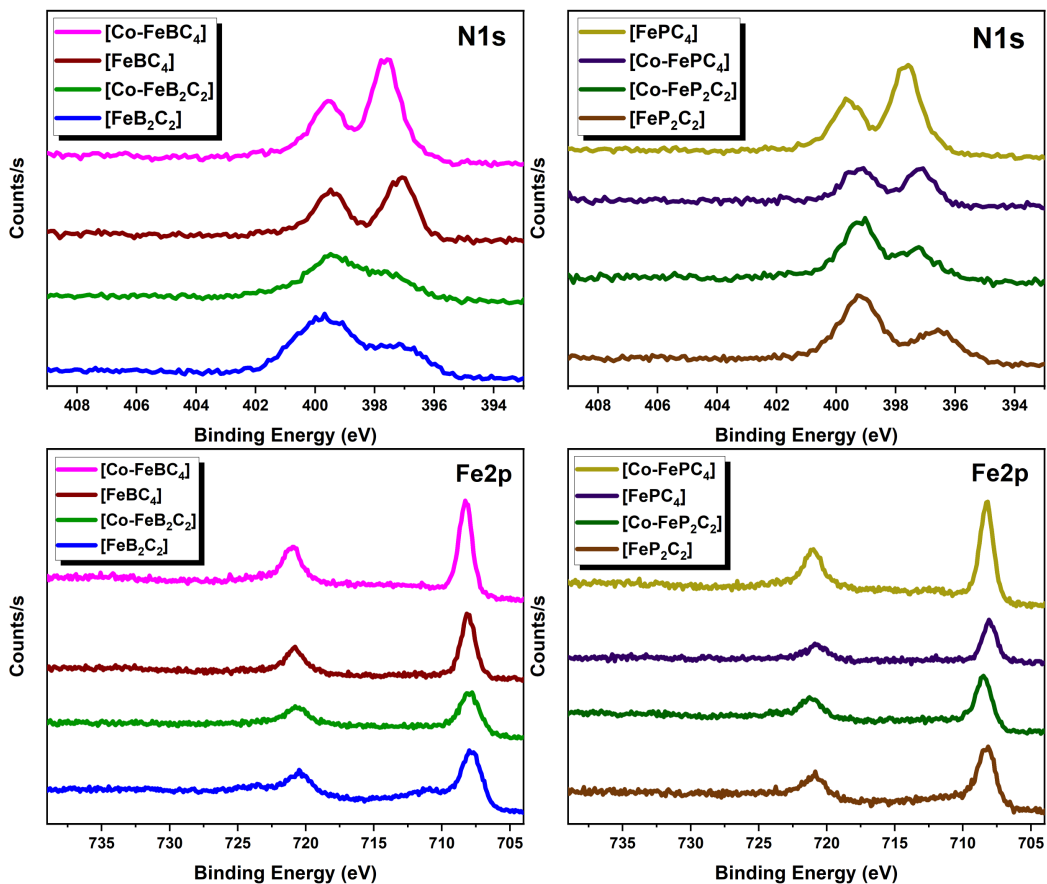


Figure 3.5: N1s and Fe2p XPS spectra of Fe-complexes and Co-Fe PBAs.

The novelty of this study emerges when cobalt is connected to iron chromophores already synthesized in 1:1 ratio producing Prussian blue analogues (PBAs). To the best of our knowledge, no such study has been reported in literature so far for water splitting application. Comparison of binding energies for Fe2p and N1s of just the chromophores and Co-Fe PBAs demonstrated the effect of cobalt.

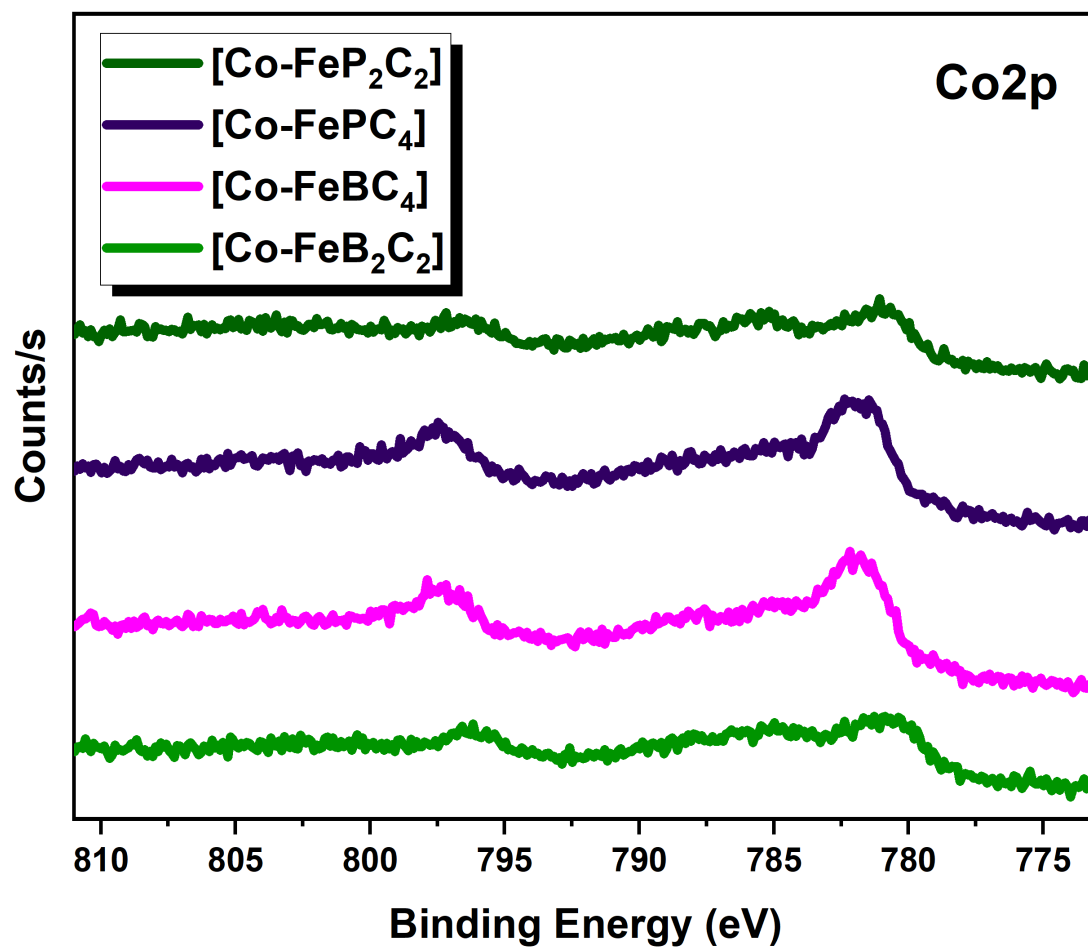


Figure 3.6: Co2p XPS spectra of of Co-Fe PBAs.

Complexes	Co ²⁺ (2p _{3/2} , 2p _{1/2}) (eV)
[Co-FeB ₂ C ₂]	796.58, 780.68
[Co-FeP ₂ C ₂]	796.68, 780.78
[Co-FeBC ₄]	797.18, 781.88
[Co-FePC ₄]	797.48, 781.98

Table 3.7: Binding energies of Co2p of Iron Chromophores.

3.4 Scanning Electron Microscopy (SEM)

In Figure 3.7, SEM images portray unique morphology of all the chromophores.

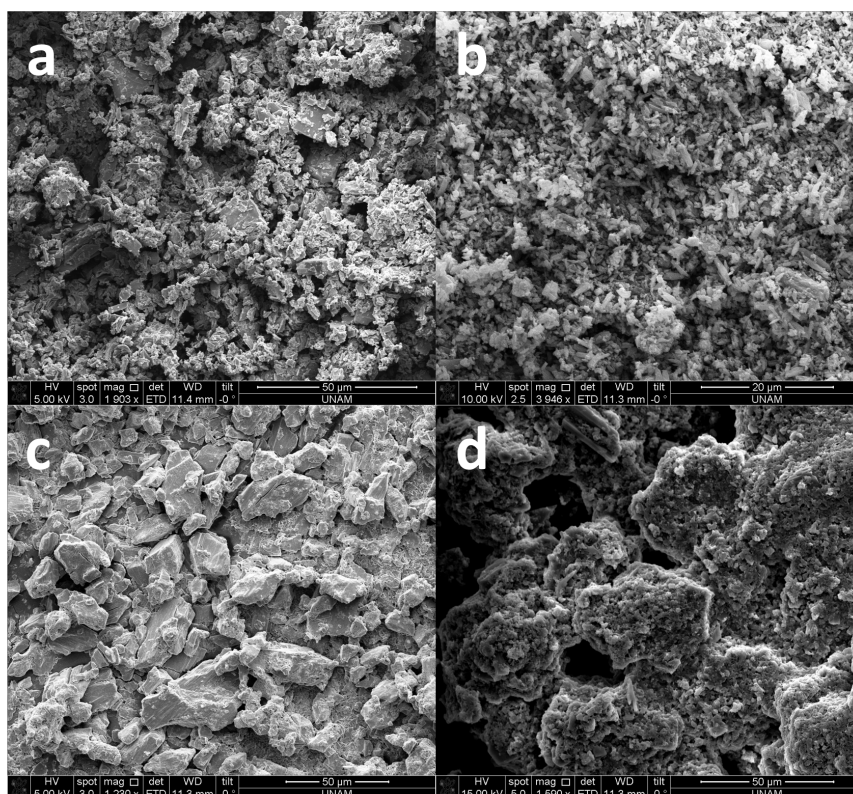


Figure 3.7: SEM images of (a) [FeB₂C₂] (b) [FeP₂C₂] (c) [FeBC₄] (d) [FePC₄].

3.5 Energy Dispersive X-Ray Analysis (EDX)

The formation of iron chromophores was further confirmed by EDX analysis. It is clearly shown in Figure 3.8 that in all the chromophores C, N and Fe elements are present. In addition, potassium (K) peaks appeared in case of tetracyano bpy/phen derivatives. Also, peaks corresponding to Au and Pd are observed as the samples were coated with Au/Pd to make the surface conductive (Figure 3.8).

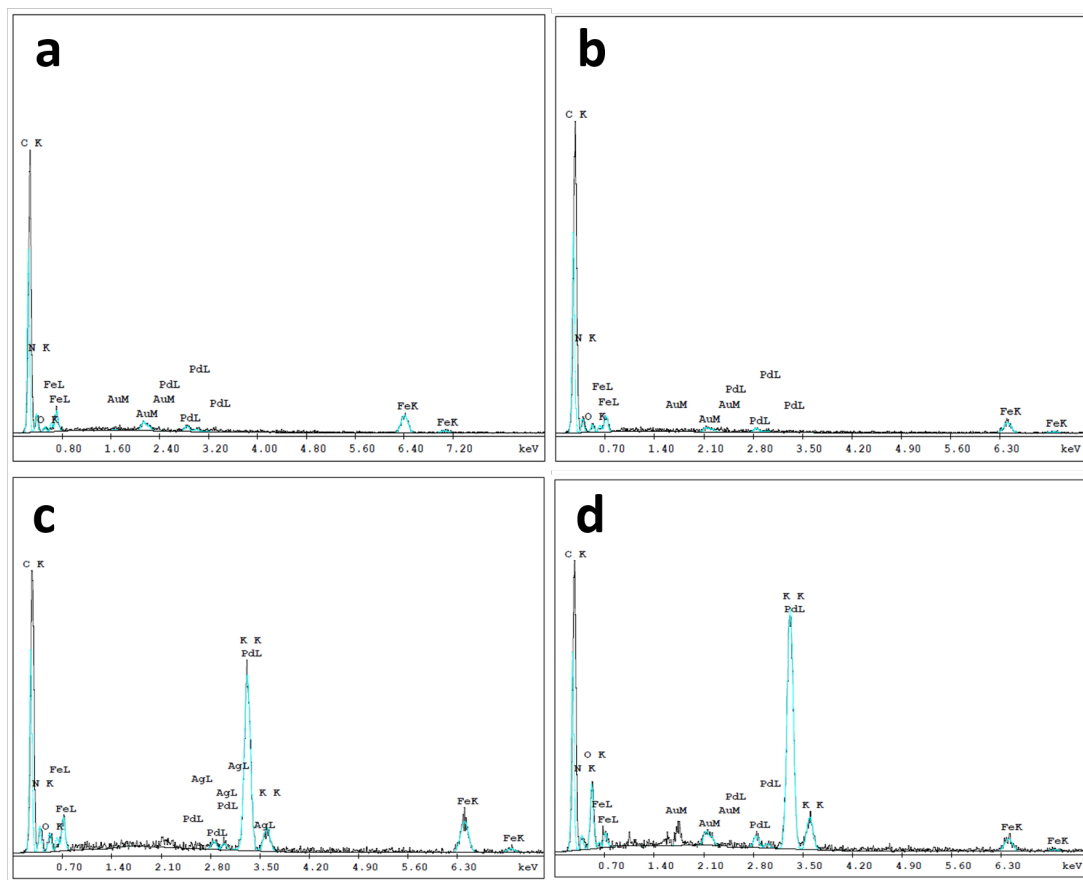


Figure 3.8: EDX analysis of (a) $[\text{FeB}_2\text{C}_2]$ (b) $[\text{FeP}_2\text{C}_2]$ (c) $[\text{FeBC}_4]$ (d) $[\text{FePC}_4]$.

The molecular formulas for Co-Fe PBAs were calculated using EDX data as follows (Table 3.8);

Complexes	Molecular Formulas
$[\text{Co-FeB}_2\text{C}_2]$	$\text{Co}_{2.47}[(\text{bpy})_2\text{Fe}(\text{CN})_2]_{3.22} \cdot (\text{Cl})_{4.94} \cdot x\text{H}_2\text{O}$
$[\text{Co-FeP}_2\text{C}_2]$	$\text{Co}_{3.03}[(\text{phen})_2\text{Fe}(\text{CN})_2]_{3.61} \cdot (\text{Cl})_{6.06} \cdot x\text{H}_2\text{O}$
$[\text{Co-FeBC}_4]$	$\text{Na}_{0.96}\text{Co}_{5.16}[(\text{bpy})\text{Fe}(\text{CN})_4]_{5.64} \cdot x\text{H}_2\text{O}$
$[\text{Co-FePC}_4]$	$\text{Co}_{5.72}[(\text{phen})\text{Fe}(\text{CN})_4]_{5.42} \cdot (\text{NO}_3)_{0.6} \cdot x\text{H}_2\text{O}$

Table 3.8: Molecular formulas of Co-Fe PBAs (powder samples) calculated using EDX % atomic ratios.

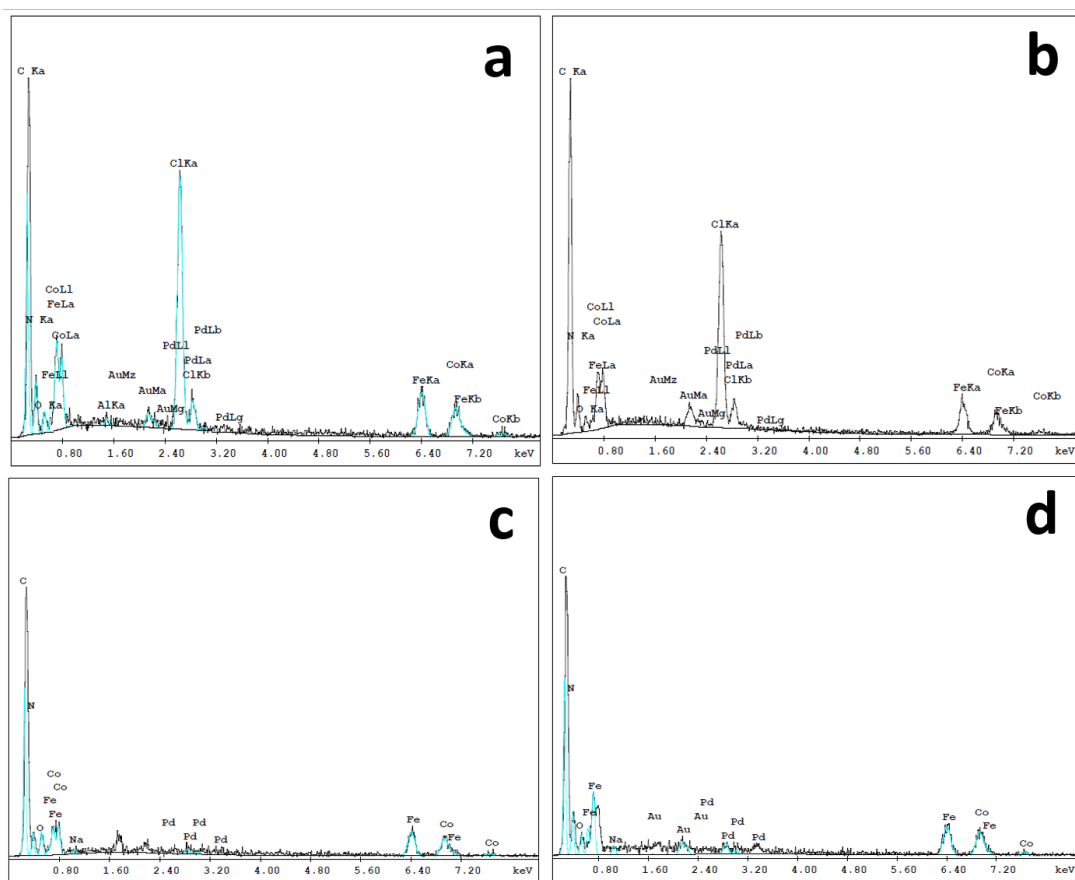


Figure 3.9: EDX analysis of (a) $[\text{Co-FeB}_2\text{C}_2]$ (b) $[\text{Co-FeP}_2\text{C}_2]$ (c) $[\text{Co-FeBC}_4]$ (d) $[\text{Co-FePC}_4]$.

3.6 Photoelectrochemical Measurements of $[\text{Co-Fe@TiO}_2/\text{FTO}]$ Photoanodes

3.6.1 Linear Sweep Voltammetry (LSV)

LSV results showed that $[\text{Co-FeB}_2\text{C}_2@\text{TiO}_2]$ and $[\text{Co-FeP}_2\text{C}_2@\text{TiO}_2]$ have lower current densities compare to their tetracyano derivatives ($[\text{Co-FeBC}_4@\text{TiO}_2]$ and $[\text{Co-FePC}_4@\text{TiO}_2]$). In order to evaluate the efficiency of iron chromophores, LSV of $[\text{Co-FePB}@\text{TiO}_2]$ electrode was also analysed where PB is $\text{K}_3[\text{Fe}(\text{CN})_6]$. Figure

3.6 illustrates the LSV curves of all these electrodes at potential 0.2 V vs RHE (1.23 V) and scan rate of 50 mV/s maintaining neutral pH. The exact Current densities produced by these electrodes at potential= 1.6 V are shown in the Table 3.9.

Complexes	Current density $\mu\text{A}/\text{cm}^2$
[Bare-TiO ₂]	25
[Co-PB@TiO ₂]	31
[Co-FeB ₂ C ₂ @TiO ₂]	45
[Co-FeP ₂ C ₂ @TiO ₂]	48
[Co-FeBC ₄ @TiO ₂]	57
[Co-FePC ₄ @TiO ₂]	61

Table 3.9: Comparison of Current Densities obtained by linear sweep voltammetry at Potential of 1.0 V vs RHE.

It is observed in Figure 3.10 that in dark [Co-PB@TiO₂] performed most efficiently however in light [Co-FeBC₄@TiO₂] and [Co-FeC₄@TiO₂] are the most efficient one with current density greater than 70 $\mu\text{A}/\text{cm}^2$.

In contrary to this, [Co-FeB₂C₂@TiO₂] and [Co-FeP₂C₂@TiO₂] lie in between, efficient than [Co-PB@TiO₂] but poorer than [Co-FeBC₄@TiO₂] and [Co-FeC₄@TiO₂] (Figure 3.11). Hence, we concluded that increasing the number of cyanide ligands increases the current density. At higher potentials (around 1.5 V) the current increases sharply due to the water oxidation by cobalt sites.

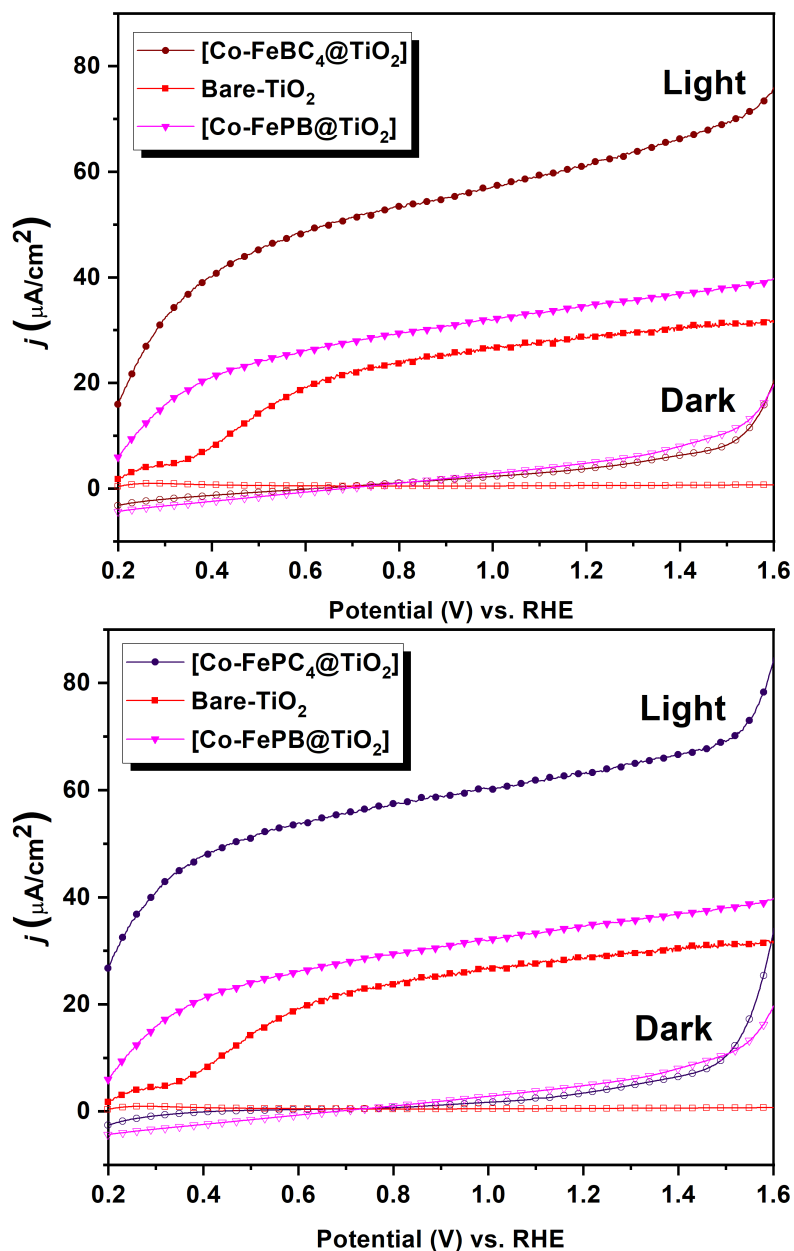


Figure 3.10: LSV curves of Bare-TiO₂ (Red, Closed square=Light, Open square=Dark), [Co-PB@TiO₂] (Pink, Closed triangle=Light, Open triangle=Dark), [Co-FeBC₄@TiO₂] (Wine, Closed circle=Light, Open circle=Dark) and [Co-FeC₄@TiO₂] (magenta, Closed circle=Light, Open circle=Dark).

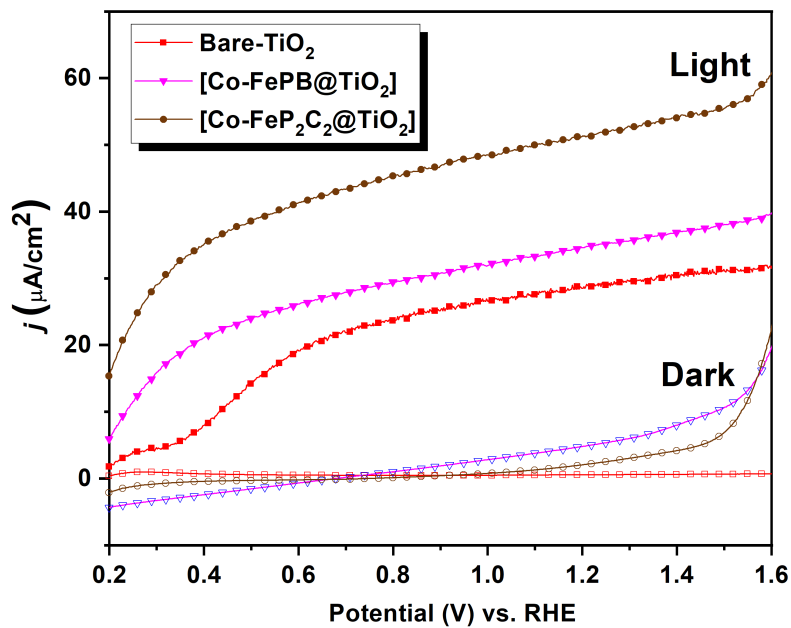
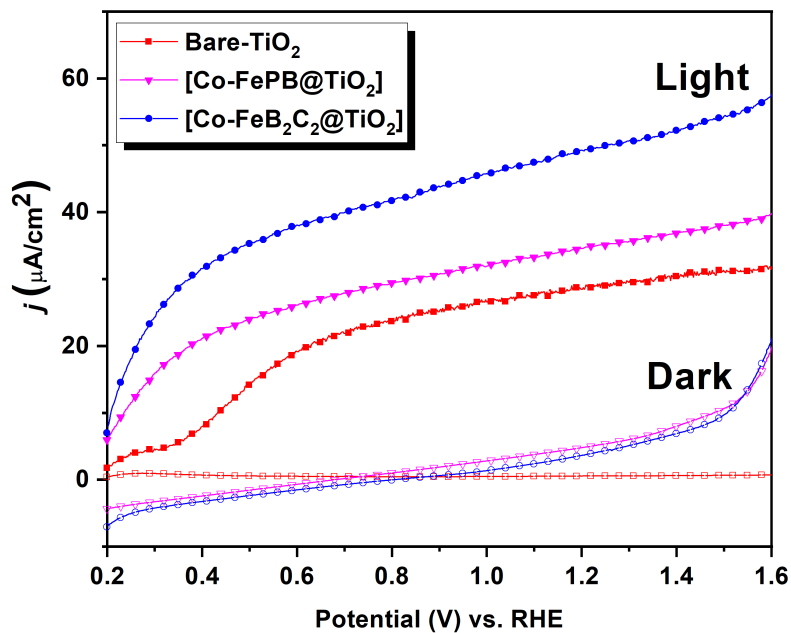


Figure 3.11: LSV curves of Bare-TiO₂ (Red, Closed square=Light, Open square=Dark), [Co-PB@TiO₂] (Pink, Closed triangle=Light, Open triangle=Dark), [Co-FeB₂C₂@TiO₂] (Blue, Closed circle=Light, Open circle=Dark) and [Co-FeP₂C₂@TiO₂] (Brown, Closed circle=Light, Open circle=Dark).

3.6.2 Chronoamperometry

To check the stability of photoanodes both short term and long term chronoamperometry was done.

3.6.2.1 Short-term Chronoamperometry

Applying the potential of 1.22 V vs RHE and keeping scan rate of 50 mV/s, stability of photoanodes was examined for 300s. All the photoanodes have shown stability for short time period (Figure 3.12). However, the current densities for [Co-FeBC₄@TiO₂] and [Co-FePC₄@TiO₂] are higher than [Co-FeB₂C₂@TiO₂] and [Co-FeP₂C₂@TiO₂], which support LSV results.

3.6.2.2 Long-term Chronoamperometry

Stability of photoanodes was also tested for longer time i.e. 2hr. Figure 3.13a clearly depicts the high stability of [Co-FeBC₄@TiO₂] versus [Co-FeB₂C₂@TiO₂], which gradually became unstable during the course of time. It can be seen in Table 3.6 that a difference of ≈ 6 or $7 \mu\text{A}$ emerged before and after the stability test supporting the fact that cobalt couldn't bind to [FeB₂C₂] and [FeP₂C₂] as strongly and efficiently (Table 3.10). This is because cyanide ligands are more competent to bind with titania surface than bpy/phen ligands thereby reducing the efficient binding of cobalt with the chromophore. Long-term chronoamperometry parameters were kept the same as for short-term chronoamperometry (1.22 V applied bias vs RHE, 50 mV/s scan rate).

*CA is a short form of Chronoamperometry where j is current density.

Photoanodes	$j(\mu\text{A}/\text{cm}^2)$ before CA	$j(\mu\text{A}/\text{cm}^2)$ after CA (2hr)
[Co-FeB ₂ C ₂ @TiO ₂]	41	33
[Co-FeP ₂ C ₂ @TiO ₂]	52	51
[Co-FeBC ₄ @TiO ₂]	40	33
[Co-FePC ₄ @TiO ₂]	53	52

Table 3.10: Difference in current densities ($\mu\text{A}/\text{cm}^2$) of (a) [Co-FeB₂C₂@TiO₂] (blue) and [Co-FeBC₄@TiO₂] (wine) (b) [Co-FeP₂C₂@TiO₂] (brown) and [Co-FePC₄@TiO₂] (magenta) before and after 2hr chronoamperometry.

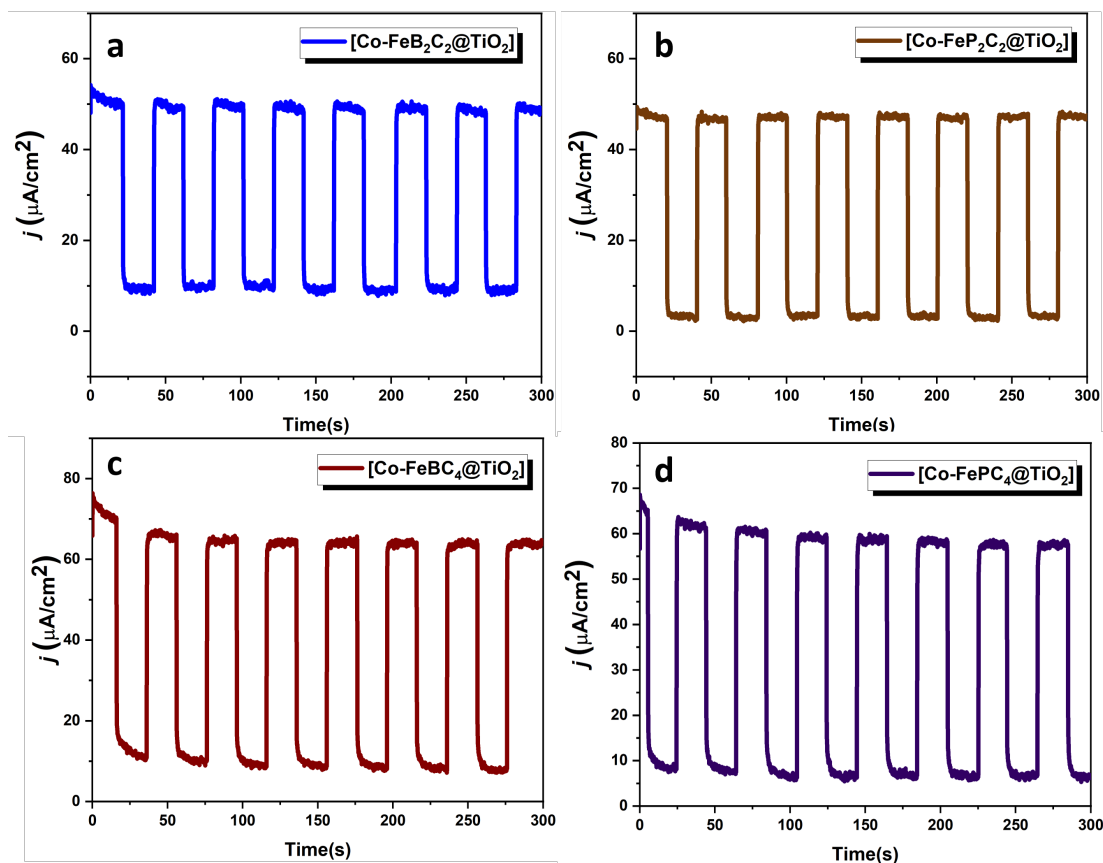


Figure 3.12: Short-term chronoamperometry (300s, $\nu=50\text{mV}/\text{s}$) (a) [Co-FeB₂C₂@TiO₂] (blue) (b) [Co-FeP₂C₂@TiO₂] (brown) (c) [Co-FeBC₄@TiO₂] (wine) (d) [Co-FePC₄@TiO₂] (magenta).

Similar current vs time profiles were observed for $[\text{Co-FeP}_2\text{C}_2@\text{TiO}_2]$ and $[\text{Co-FePC}_4@\text{TiO}_2]$ (Figure 3.13). Current density remained almost constant for 2hr indicating the sustainability of $[\text{FePC}_4\text{-Co}]$ over TiO_2 surface. However, $[\text{FePC}_4\text{-Co}]$ Prussian blue analogue (PBA) started to fall off the TiO_2 surface with time proving it's inefficiency for water oxidation.

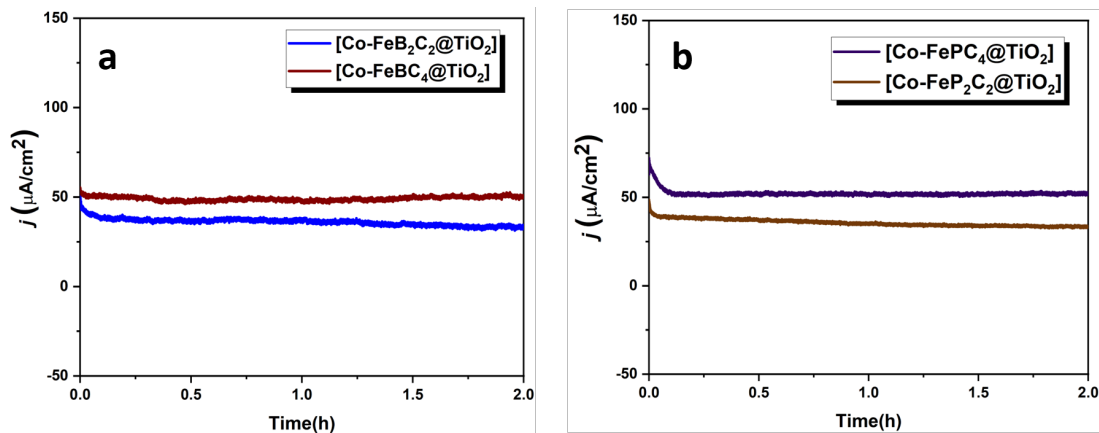


Figure 3.13: Long-term chronoamperometry (2hr, $\nu=50$ mV/s, $V=1.22$ volts versus RHE) (a) $[\text{Co-FeB}_2\text{C}_2@\text{TiO}_2]$ (blue), $[\text{Co-FeBC}_4@\text{TiO}_2]$ (wine) (b) $[\text{Co-FeP}_2\text{C}_2@\text{TiO}_2]$ (brown), $[\text{Co-FePC}_4@\text{TiO}_2]$ (magenta).

3.7 Post-Catalytic Characterization

3.7.1 Linear Sweep Voltammetry (LSV)

After 2hr of extensive stability test of PBA modified TiO_2 coated FTO, current density was measured again via LSV to validate the efficiency of these electrodes. It is signified from the Figure 3.14 the endurance and longevity of $[\text{Co-FeBC}_4@\text{TiO}_2]$ and $[\text{Co-FePC}_4@\text{TiO}_2]$ electrodes even after 2hr of chronoamperometry. This revealed that iron complexes with four cyanide ligands can coordinate better with cobalt bringing out PBA with better performance toward oxidation of water. This is in good consensus with long-term chronoamperometry results.

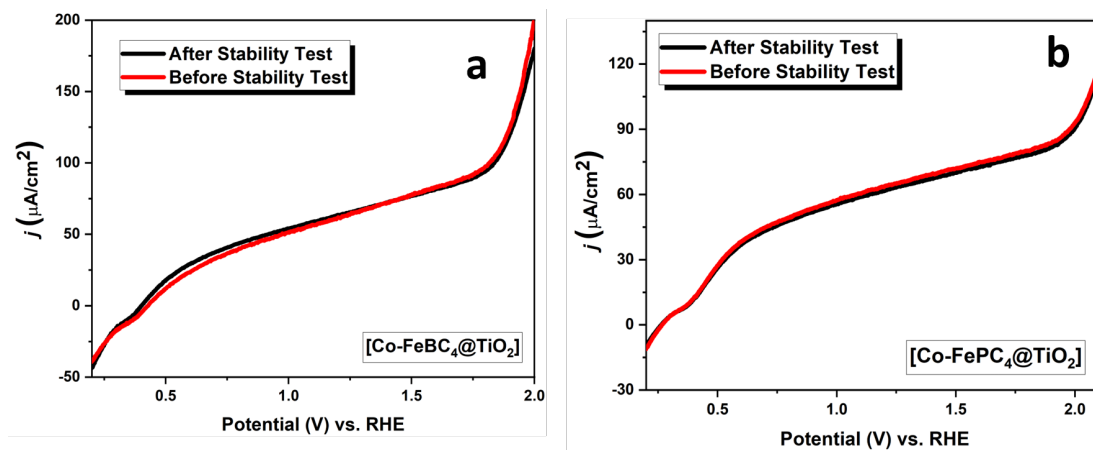


Figure 3.14: Post-catalytic LSV (0.2-2.0 V versus RHE, $\nu=50$ mV/s), (a) [Co-FeBC₄@TiO₂], (b) [Co-FePC₄@TiO₂], Red=Before stability test, Black=After stability test.

In contrary to this, [Co-FeB₂C₂@TiO₂] and [Co-FeP₂C₂@TiO₂] showed obvious decomposition subsequent to stability test supporting long-term chronoamperometry results. This developed an evident comprehension that iron complexes having two cyanide ligands are unable to hold the cobalt catalyst thereby declining the efficiency of photoanodes. It can be seen in the Figure 3.15 that current density at higher potential is lower after stability test, attributed to decrease in water oxidation cobalt sites due to decomposition of PBA over titania surface.

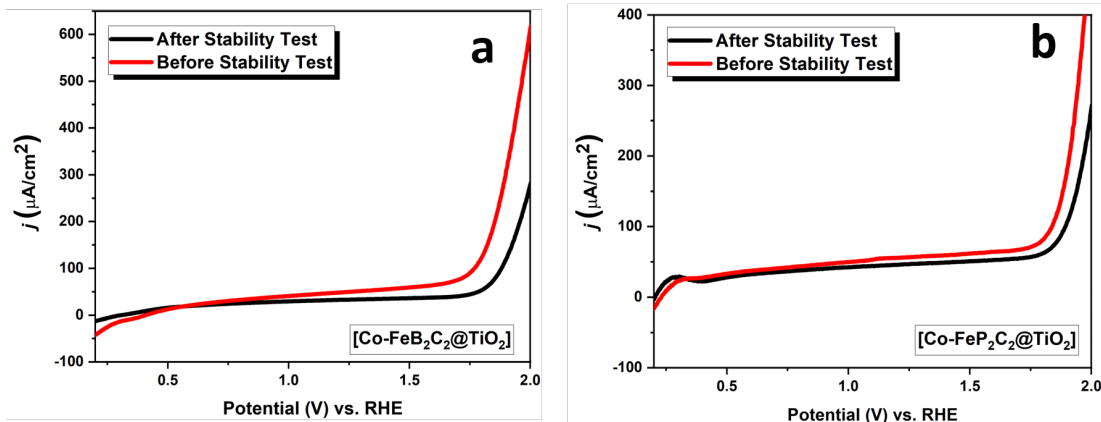


Figure 3.15: Post-catalytic LSV (0.2-2 V vs RHE, $\nu=50$ mV/s), (a) [Co-FeB₂C₂@TiO₂], (b) [Co-FeP₂C₂@TiO₂], Red=Before stability test, Black=After stability test.

3.7.2 X-Ray Photoelectron Spectroscopy (XPS)

Figure 3.16 represents the Co2p spectra recorded for pristine and postcatalytic photoanodes. Altogether, similar profiles are observed for each case. Two dominant bands are located at around 781 eV and 797 eV for 2p_{1/2} and 2p_{3/2} revealed the presence of Co²⁺ in both pristine and postcatalytic [Co-FeBC₄@TiO₂] and [Co-FePC₄@TiO₂]. Also peaks characteristic to Co³⁺ are also present with satellite bands displaying a descent stability of [Co-FeBC₄@TiO₂] and [Co-FePC₄@TiO₂] toward photoelectrochemical water oxidation process (Figure 3.16, 3.17) [60]. However, Co³⁺ has signal enhancement in postcatalytic samples, which showed partial oxidation of cobalt sites during water oxidation process. Exact peaks position in eV is shown in Table 3.11. [56] [58] [69]. Moreover, the formation of thermodynamically stable Co₃O₄ is eminent by a dominant band located below or close to 780 eV [69] [58] [44], which is absent in our case. Therefore, this rationalize the stability of our photoanodes which does not show any decomposition to cobalt oxide.

Complexes	Co ²⁺ (2p _{1/2} , 2p _{3/2}) pristine	Co ²⁺ (2p _{1/2} , 2p _{3/2}) postcatalytic
[Co-FeBC ₄]	781.58 eV, 797.18 eV	781.78 eV, 797.28 eV
[Co-FePC ₄]	781.68 eV, 797.38 eV	781.59 eV, 797.39 eV

Table 3.11: Binding Energies of Co2p of pristine and postcatalytic electrodes.

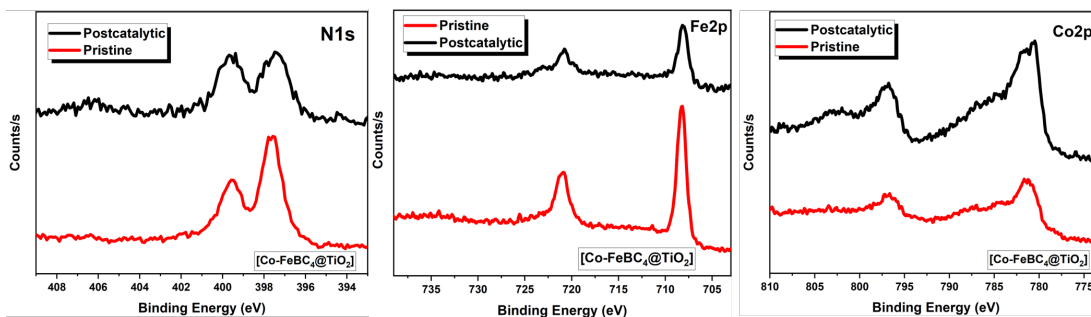


Figure 3.16: Pristine and Postcatalytic XPS of [Co-FeBC₄@TiO₂], Red=Pristine, Black=Postcatalytic.

N1s region of pristine and postcatalytic samples of both the electrodes showed peaks at approximately 399 eV and 397 eV corresponding to CN of phen/bpy ligands (Table 3.12) and CN linked to cobalt catalyst shown in the Figure 3.16 and 3.17 [56] [58] [69] [68].

Complexes	N1s (eV) Pristine	N1s (eV) postcatalytic
[Co-FeBC ₄]	397.58, 399.58	397.48, 399.68
[Co-FePC ₄]	397.58, 399.88	397.77, 39.87

Table 3.12: Binding Energies of N1s of pristine and postcatalytic electrodes.

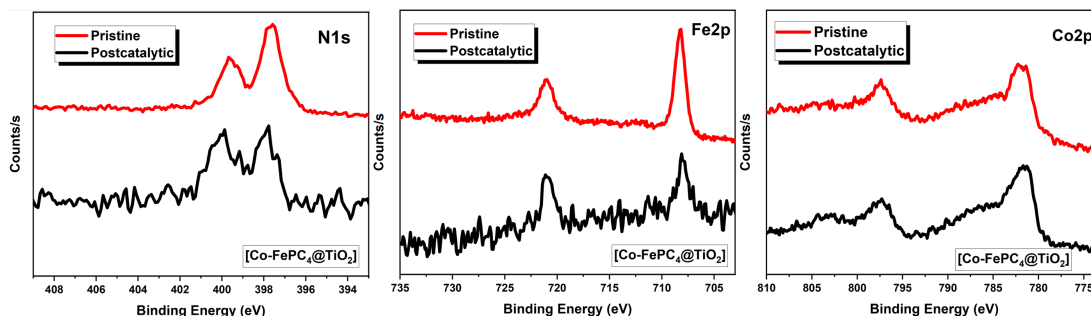


Figure 3.17: Pristine and Postcatalytic XPS of $[\text{Co-FePC}_4@\text{TiO}_2]$, Red=Pristine, Black=Postcatalytic.

Comparison of Fe2p XPS spectra of photoanodes before and after photoelectrocatalytic measurements are shown in Figure 3.16 and 3.17. Similar to pristine samples, two ruling peaks at binding energies of approximately 708 eV and 720 eV represent $2p_{3/2}$ and $2p_{1/2}$ of Fe^{2+} while two smaller bands at around 709 eV and 723 eV might be present attributed to the presence of Fe^{2+} to Fe^{3+} ions in $[\text{Fe}(\text{CN})_4]^{2-}$ fragment. The similarity in XPS spectra of pristine and postcatalytic further justify the stability of photoanodes (Table 3.13) [59] [68].

Complexes	$\text{Fe}^{2+}(2p_{1/2}, 2p_{3/2})$ pristine	$\text{Fe}^{2+}(2p_{1/2}, 2p_{3/2})$ postcatalytic
$[\text{Co-FeBC}_4]$	720.97 eV, 708.28 eV	720.78 eV, 708.18 eV
$[\text{Co-FePC}_4]$	721.08 eV, 708.18 eV	721.11 eV, 708.11 eV

Table 3.13: Binding Energies of Fe2p of pristine and postcatalytic electrodes.

3.7.3 Scanning Electron Microscopy (SEM) and Energy Dispersive X-ray Analysis (EDX)

SEM images of $[\text{CoFe-coat}@\text{TiO}_2/\text{FTO}]$ indicate that PBA retained continuous film over titania surface even after photoelectrocatalytic water oxidation process (Figure 3.18).

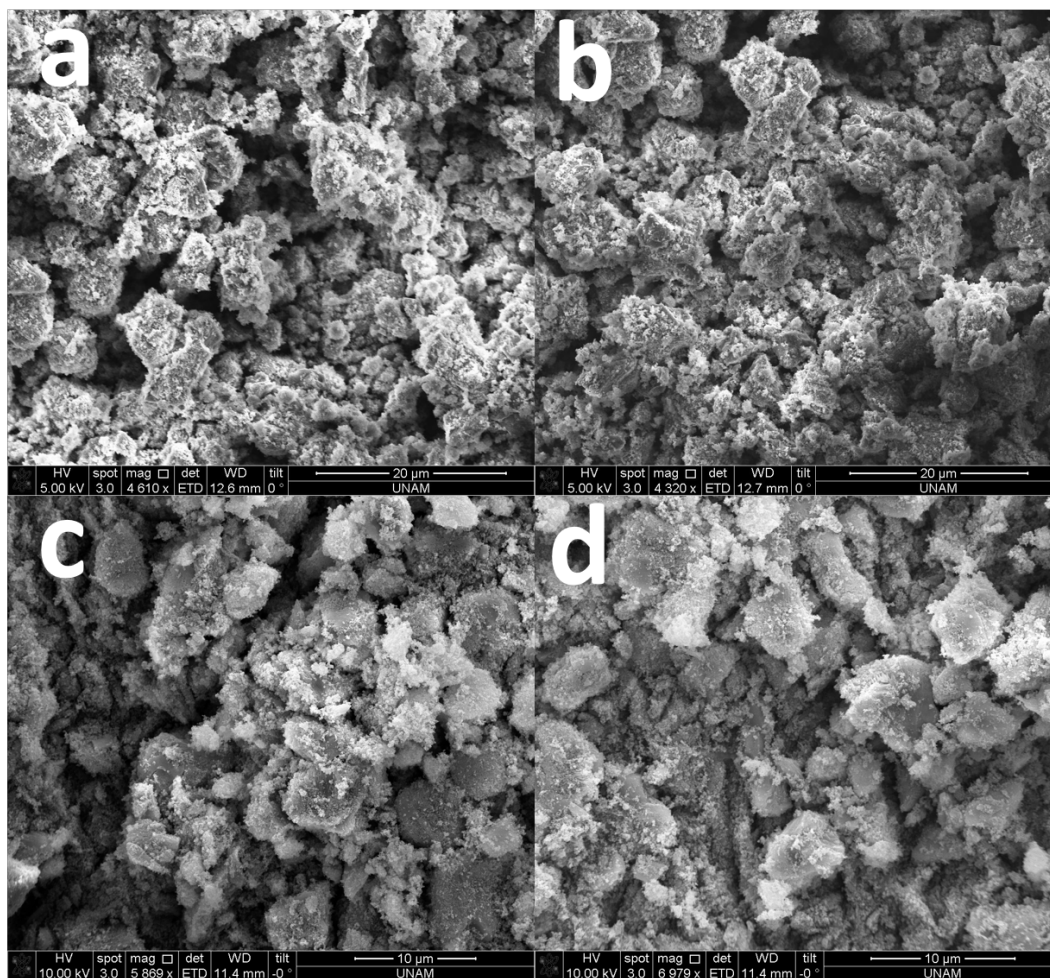


Figure 3.18: SEM images of (a) [Co-FeBC₄] PBA pristine, (b) [Co-FeBC₄] PBA postcatalytic, (c) [Co-FePC₄] PBA pristine, (d) [Co-FePC₄] PBA postcatalytic.

Molecular formulas are calculated based on EDX results (Figure 3.19) to see the Co:Fe ratios in PBA. The Co:Fe ratios are almost 1:1 in postcatalytic samples. The molecular formulas are mentioned the Table 3.14.

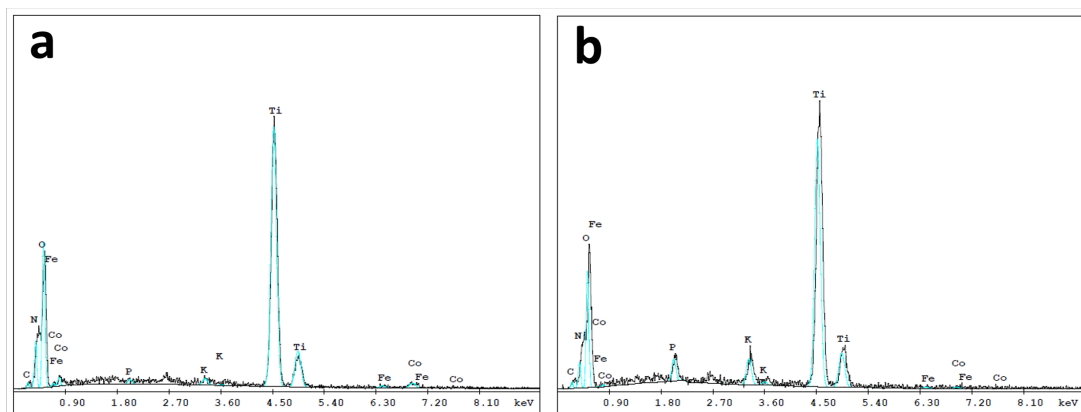


Figure 3.19: EDX analysis of (a) $[\text{Co-FeBC}_4@\text{TiO}_2]$ postcatalytic, (b) $[\text{Co-FePC}_4@\text{TiO}_2]$ postcatalytic.

Photoanodes	Molecular Formulas
$[\text{Co-FeBC}_4@\text{TiO}_2]$	$\text{Co}_{1.2}[(\text{bpy})\text{Fe}(\text{CN})_4] \cdot (\text{NO}_3)_{0.4} \cdot x\text{H}_2\text{O}$
$[\text{Co-FePC}_4@\text{TiO}_2]$	$\text{Co}_{1.3}[(\text{phen})\text{Fe}(\text{CN})_4] \cdot (\text{NO}_3)_{0.6} \cdot x\text{H}_2\text{O}$

Table 3.14: Molecular formulas of $[\text{Co-Fe}/\text{TiO}_2]$ (post-catalytic) calculated using EDX % atomic ratios.

3.7.4 Incident Photon to Current Efficiency (IPCE)

For incident photon-to-current conversion efficiency (IPCE) measurement, light from the Xenon lamp was dispersed by a monochromator and the photocurrent was recorded at a constant bias (1.23 V vs RHE) with a spectral step of 10 nm. This light is entered into a monochromator (Oriel 1/8 m cornerstone, 1200 *lines/mm* grating) and the output of the monochromator is illuminated onto the photoanode in three-electrode setup. The current was recorded using a computer-controlled setup consisting of potentiostat (CH instrument). The dark and under illumination current values for different incident light wavelengths are measured. To find the portion of photocurrent, these two current amounts are subtracted.

To calculate the IPCE, the following equation was used:

$$IPCE(\%) = \frac{1240}{\lambda} \times \frac{j}{P_{light}} \times 100 \quad (3.1)$$

where j is the photocurrent density (mA/cm^2), λ is the incident light wavelength (nm) from monochromatic light, P_{light} is the power density of monochromatic light at a specific wavelength (mW/cm^2).

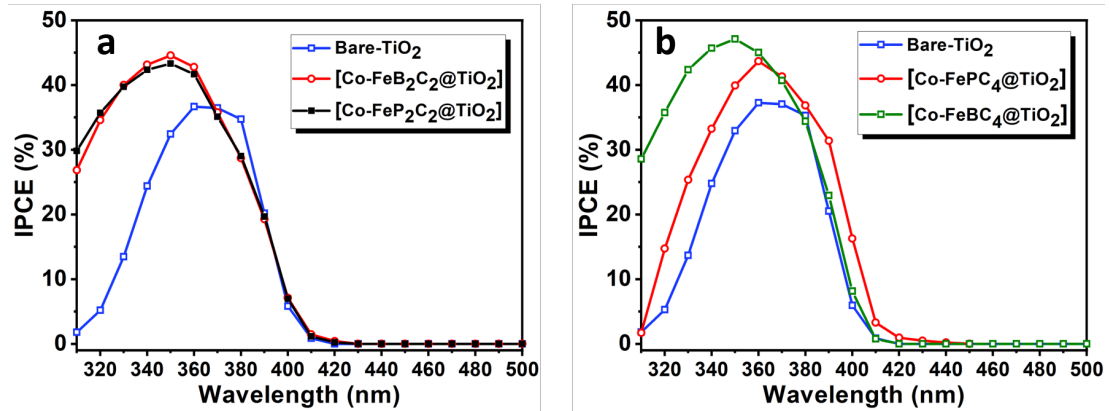


Figure 3.20: IPCE (%) of (a) [Co-FeB₂C₂@TiO₂], [Co-FeP₂C₂@TiO₂], (b) [Co-FeBC₄@TiO₂], [Co-FePC₄@TiO₂].

Dye molecules have dominant absorption between 300-350 nm. That is why IPCE data shows considerable improvement. For [Co-B₂C₂@TiO₂] and [Co-BC₄@TiO₂] samples, a local maximum is observed at around 360 nm, seen from UV-Vis spectra. Therefore, the IPCE reaches its maximum at this spectral position. For [Co-P₂C₂@TiO₂] and [Co-PC₄@TiO₂] samples, a weak but broad absorption is probed from 370 nm to 580 nm. From IPCE data, the absorption in this regime leads to photocurrent generation at wavelengths above 410 nm where TiO₂ is inactive (Figure 3.19).

3.7.5 Band Alignment Interpretation

Finally, to see the reliability of our results band alignments of all the photoanodes were assigned. Briefly, band gap of titania is already reported in our previous

study. So, the band gaps of our Co-Fe PBAs are calculated using their UV-Vis absorption profiles specifically MLCT band wavelengths. Also, the energy of HOMO (highest occupied molecular orbital) level is taken from the onset potential of dark LSV already recorded for all the photoanodes. As expected, [Co-FePC₄@TiO₂] has lower LUMO (lowest unoccupied molecular orbital) level (-0.92 eV) than LUMO of [Co-FeBC₄@TiO₂] which is located at -1.01 eV. This supports IPCE results where [Co-FeBC₄@TiO₂] absorbs less than [Co-FePC₄@TiO₂] (Figure 3.21).

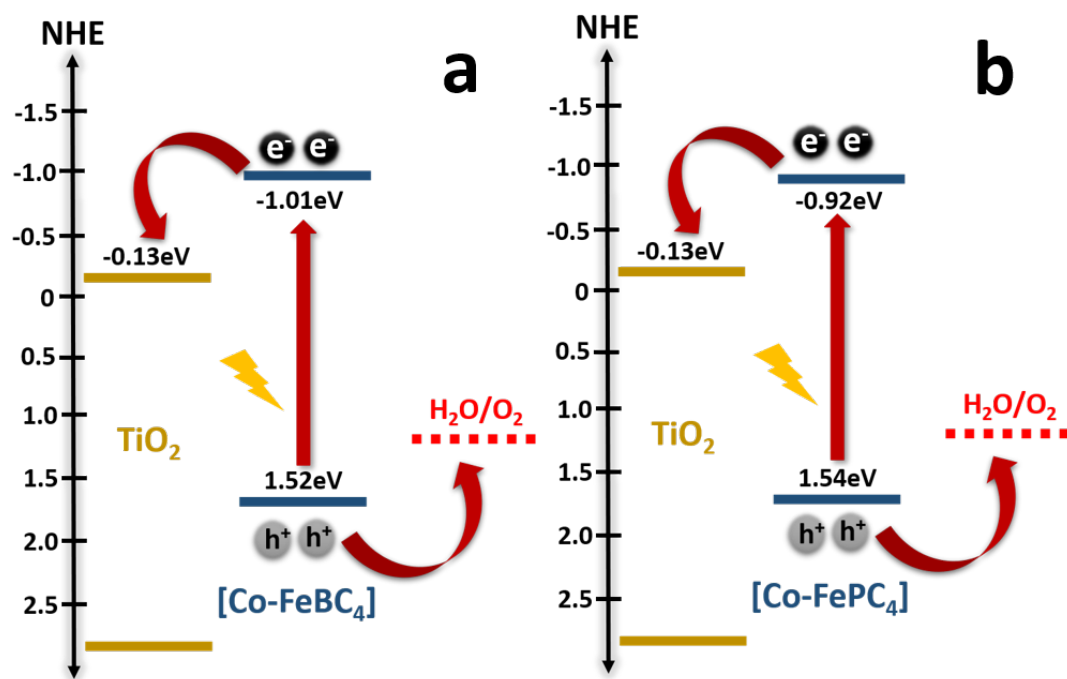


Figure 3.21: Band diagram for (a) [Co-FeBC₄@TiO₂], (b) [Co-FePC₄@TiO₂], arrows show the movement of charges after illumination.

Contrary to this, LUMO levels of [Co-FeP₂C₂@TiO₂] and [Co-FeB₂C₂@TiO₂] are much lower and their positions are not suitable enough with respect to conduction band (CB) of titania for efficient electron transfer [23] (Figure 3.22). Overall, the ³MLCT state is not suitable for sensitization of titania as explained by Jakubikova *et al.* [23] [20]. Conversely, we have also associated cobalt with iron chromophores which makes it efficient for electron transfer as well as reduces

charge recombination.

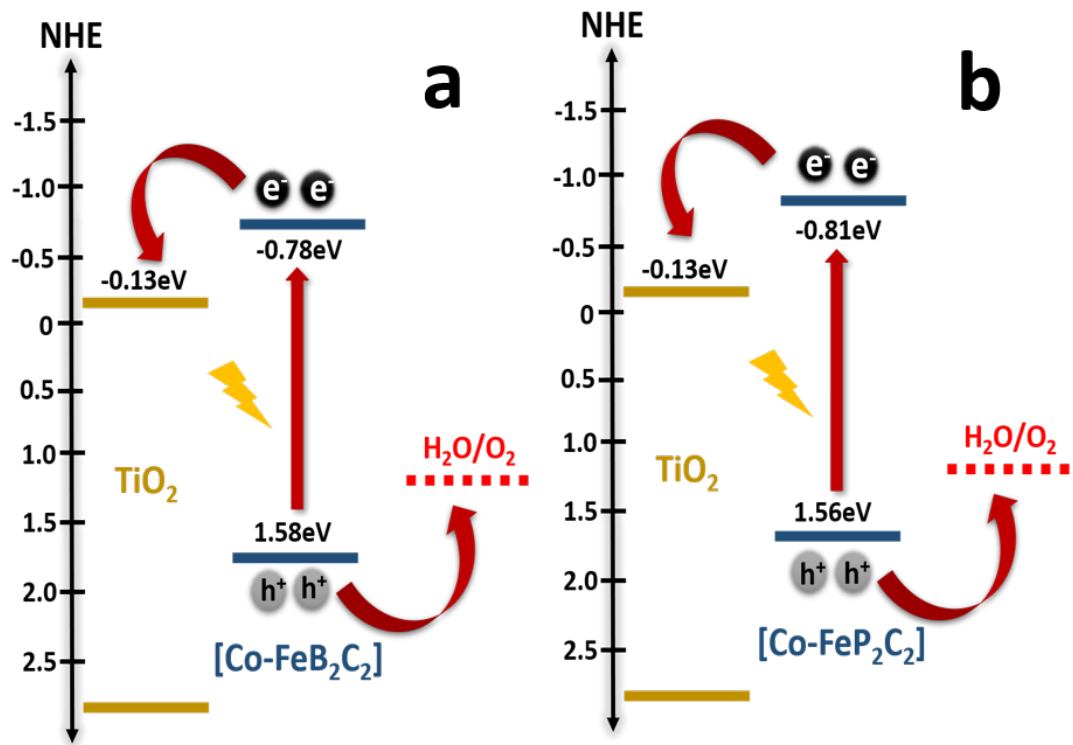


Figure 3.22: Band diagram for (a) [Co-FeB₂C₂@TiO₂], (b) [Co-FeP₂C₂@TiO₂], arrows show the movement of charges after illumination.

Chapter 4

Conclusion

Photoelectrochemical water splitting is considered as a promising pathway for solar-to-hydrogen fuel conversion with increased efficiency and effective in cost. Combined efforts have been put to improve the efficiency via enhanced light absorption and greater surface catalysis. In this thesis, low cost, efficient and earth abundant transition metal based complexes have been employed as chromophores for oxidizing water to oxygen in water splitting application.

The first and foremost approach of this project was the synthesis and characterization of iron chromophores. The synthetic methods introduced here are the simplest with no toxic by-products formation compared to previously reported comprehensive procedures [64]. This study presented novel heterogeneous photoanodes composed of iron chromophores, acting as a bridge between semiconductor and water oxidation catalyst. Presumably, this is the first study utilising stable [FeBC₄-Co] and [FePC₄-Co] Prussian blue analogues for oxidation of water. The confirmation of these iron chromophores as well as the formation of their Prussian blue analogues was accomplished gradually through multiple characterizations such as UV-Vis, FTIR, and XPS, etc. EDX analysis revealed the formation of non-stoichiometric Co-Fe Prussian blue analogues roughly 1:1 ratio in powdered samples and those over titania surface.

The main objective of this thesis began with the photoanode fabrication and its optimization. The principal outcome of the study is to come up with the stable, robust, and cost effective photoanodes. Linear sweep voltammetry results declare the exhibition of maximum current densities in [Co-FeBC₄@TiO₂] and [Co-FePC₄@TiO₂] compared to [Co-FeB₂C₂@TiO₂], [Co-FeP₂C₂@TiO₂], and [Co-PB@TiO₂] electrodes. This has established the concept of better interaction of [FeBC₄] and [FePC₄] with cobalt as well as to titania surface overall forming a stable structure. This is further validated by short term and long term chronoamperometry. Altogether, all the photoanodes were stable for 300s while the profiles differ when tested for 2 hours. As mentioned earlier, [Co-FeBC₄@TiO₂] and [Co-FePC₄@TiO₂] showed stability over the entire time period. However, [Co-FeB₂C₂@TiO₂] and [Co-FeP₂C₂@TiO₂] showed decomposition in the course of time.

The vital edge is the absence of [Co-FeBC₄@TiO₂] and [Co-FePC₄@TiO₂] decomposition to possible cobalt oxide product, confirmed by performing XPS analysis on them [69] [58] [44]. Besides, postcatalytic LSV results proved that PBA ([FePC₄-Co] and [FeBC₄-Co]) retained its morphology and stability. As oppose to this [FeB₂C₂-Co] and [FeP₂C₂-Co] has different LSV profiles as cobalt started to get off the PBA structure reducing efficiency. So we can say that strong σ -donating ability of cyanide ligands can be used to tune the MLCT energy levels which in-turn contribute to reinforce the electron transfer efficiency [38].

Another key point to be considered is that increase in current density either due to chromophore or just the catalyst could not be declared by LSV results. So for this purpose, IPCE analysis was recorded for all these photoanodes. Lastly, the band diagrams of all the photoanodes showed that [Co-FeBC₄@TiO₂] and [Co-FePC₄@TiO₂] have better band alignment than [Co-FeB₂C₂@TiO₂] and [Co-FeP₂C₂@TiO₂] electrodes as cobalt does not show effective binding in them.

To sum up, the proposed photoanodes are not that much efficient for water oxidation due to certain limitations, but it can provide a pathway toward the development of more efficient photoanodes. This could be done by introducing more strong field ligands in the structure to improve the stability, efficiency as

well as robustness.

Bibliography

- [1] F. H. Sobrino, C. R. Monroy, and J. L. H. Pérez, “Critical analysis on hydrogen as an alternative to fossil fuels and biofuels for vehicles in europe,” *Renewable and Sustainable Energy Reviews*, vol. 14, no. 2, pp. 772 – 780, 2010.
- [2] P. Sharma and M. L. Kolhe, “Review of sustainable solar hydrogen production using photon fuel on artificial leaf,” *International Journal of Hydrogen Energy*, vol. 42, no. 36, pp. 22704–22712, 2017. Exported from <https://app.dimensions.ai> on 2019/02/04.
- [3] K. Hassmann and H.-M. Kühne, “Primary energy sources for hydrogen production,” *International Journal of Hydrogen Energy*, vol. 18, no. 8, pp. 635 – 640, 1993.
- [4] J. A. Turner, “Sustainable hydrogen production,” vol. 305, no. 5686, pp. 972–974, 2004.
- [5] J. Holladay, J. Hu, D. King, and Y. Wang, “An overview of hydrogen production technologies,” *Catalysis Today*, vol. 139, no. 4, pp. 244 – 260, 2009. Hydrogen Production - Selected papers from the Hydrogen Production Symposium at the American Chemical Society 234th National Meeting Exposition, August 19-23, 2007, Boston, MA, USA.
- [6] M. Eisenstadt and K. Cox, “Hydrogen production from solar energy,” *Solar Energy*, vol. 17, no. 1, pp. 59 – 65, 1975.

- [7] A. J. Bard and M. A. Fox, “Artificial photosynthesis: solar splitting of water to hydrogen and oxygen,” *Accounts of Chemical Research*, vol. 28, no. 3, pp. 141–145, 1995.
- [8] T. J. Jacobsson, “Photoelectrochemical water splitting: an idea heading towards obsolescence?,” *Energy Environ. Sci.*, vol. 11, pp. 1977–1979, 2018.
- [9] Z. Yu, F. Li, and L. Sun, “Recent advances in dye-sensitized photoelectrochemical cells for solar hydrogen production based on molecular components,” *Energy Environ. Sci.*, vol. 8, pp. 760–775, 2015.
- [10] W. J. Youngblood, S.-H. A. Lee, K. Maeda, and T. E. Mallouk, “Visible light water splitting using dye-sensitized oxide semiconductors,” *Accounts of Chemical Research*, vol. 42, no. 12, pp. 1966–1973, 2009. PMID: 19905000.
- [11] J. Jia, L. C. Seitz, J. D. Benck, Y. Huo, Y. E. Chen, J. W. D. Ng, T. Bilir, J. S. Harris, and T. F. Jaramillo, “Solar water splitting by photovoltaic-electrolysis with a solar-to-hydrogen efficiency over 30%,” *Nature communications*, 2016.
- [12] M. Watanabe, “Dye-sensitized photocatalyst for effective water splitting catalyst,” *Science and Technology of Advanced Materials*, vol. 18, pp. 705–723, 12 2017.
- [13] X. Ding, L. Zhang, Y. Wang, A. Liu, and Y. Gao, “Design of photoanode-based dye-sensitized photoelectrochemical cells assembling with transition metal complexes for visible light-induced water splitting,” *Coordination Chemistry Reviews*, vol. 357, pp. 130 – 143, 2018.
- [14] C. A. Bignozzi, R. Argazzi, and C. J. Kleverlaan, “Molecular and supramolecular sensitization of nanocrystalline wide band-gap semiconductors with mononuclear and polynuclear metal complexes,” *Chemical Society Reviews*, vol. 29, no. 2, pp. 87–96, 2000.
- [15] M. Grätzel, “Dye-sensitized solar cells,” *Journal of Photochemistry and Photobiology C: Photochemistry Reviews*, vol. 4, no. 2, pp. 145 – 153, 2003.

- [16] P. G. Bomben, K. C. Robson, B. D. Koivisto, and C. P. Berlinguette, “Cyclometalated ruthenium chromophores for the dye-sensitized solar cell,” *Coordination Chemistry Reviews*, vol. 256, no. 15, pp. 1438 – 1450, 2012. 19th International Symposium on the Photophysics and Photochemistry of Coordination Compounds.
- [17] “Design and development of functionalized cyclometalated ruthenium chromophores for light-harvesting applications,” *INORGANIC CHEMISTRY*, vol. 50, pp. 5494–5508, JUN 20 2011.
- [18] M. R. Norris, J. J. Concepcion, Z. Fang, J. L. Templeton, and T. J. Meyer, “Low-overpotential water oxidation by a surface-bound ruthenium-chromophore–ruthenium-catalyst assembly,” *Angewandte Chemie International Edition*, vol. 52, no. 51, pp. 13580–13583.
- [19] D. L. Ashford, M. K. Gish, A. K. Vannucci, M. K. Brennaman, J. L. Templeton, J. M. Papanikolas, and T. J. Meyer, “Molecular chromophore–catalyst assemblies for solar fuel applications,” *Chemical Reviews*, vol. 115, no. 23, pp. 13006–13049, 2015. PMID: 26513130.
- [20] E. Jakubikova and D. N. Bowman, “*Fe(II)*-polypyridines as chromophores in dye-sensitized solar cells: A computational perspective,” *Accounts of Chemical Research*, vol. 48, no. 5, pp. 1441–1449, 2015. PMID: 25919490.
- [21] Y. Liu, P. Persson, V. Sundström, and K. Wärnmark, “Fe *n*-heterocyclic carbene complexes as promising photosensitizers,” *Accounts of Chemical Research*, vol. 49, no. 8, pp. 1477–1485, 2016. PMID: 27455191.
- [22] K. S. Kjær, W. Zhang, R. Alonso-Mori, U. Bergmann, M. Chollet, R. G. Hadt, R. W. Hartsock, T. Harlang, T. Kroll, K. Kubiček, H. T. Lemke, H. W. Liang, Y. Liu, M. M. Nielsen, J. S. Robinson, E. I. Solomon, D. Sokaras, T. B. van Driel, T.-C. Weng, D. Zhu, P. Persson, K. Wärnmark, V. Sundström, and K. J. Gaffney, “Ligand manipulation of charge transfer excited state relaxation and spin crossover in $[Fe(2,2\text{-bipyridine})_2(CN)_2]$,” journal = *Structural Dynamics*, volume = 4, number = 4, pages = 044030, year = 2017, doi = 10.1063/1.4985017, url = <https://doi.org/10.1063/1.4985017> , eprint = <https://doi.org/10.1063/1.4985017> ,”

- [23] D. N. Bowman, J. H. Blew, T. Tsuchiya, and E. Jakubikova, "Elucidating band-selective sensitization in iron(II) polypyridine- TiO_2 assemblies," *Inorganic Chemistry*, vol. 52, no. 15, pp. 8621–8628, 2013. PMID: 23837840.
- [24] D. N. Bowman, S. Mukherjee, L. J. Barnes, and E. Jakubikova, "Linker dependence of interfacial electron transfer rates in $Fe(II)$ -polypyridine sensitized solar cells," *Journal of Physics: Condensed Matter*, vol. 27, p. 134205, mar 2015.
- [25] S. Mukherjee, D. N. Bowman, and E. Jakubikova, "Cyclometalated $Fe(II)$ complexes as sensitizers in dye-sensitized solar cells," *Inorganic Chemistry*, vol. 54, no. 2, pp. 560–569, 2015. PMID: 25531506.
- [26] I. M. Dixon, F. Alary, M. Boggio-Pasqua, and J.-L. Heully, "The $(N_4C_2)^{2-}$ donor set as promising motif for bis(tridentate) iron(II) photoactive compounds," *Inorganic Chemistry*, vol. 52, no. 23, pp. 13369–13374, 2013.
- [27] Y. Liu, T. Harlang, S. E. Canton, P. Chábera, K. Suárez-Alcántara, A. Fleckhaus, D. A. Vithanage, E. Göransson, A. Corani, R. Lomoth, V. Sundström, and K. Wärnmark, "Towards longer-lived metal-to-ligand charge transfer states of *iron(ii)* complexes: an *n*-heterocyclic carbene approach," *Chem. Commun.*, vol. 49, pp. 6412–6414, 2013.
- [28] P. Chábera, K. S. Kjaer, O. Prakash, A. Honarfar, Y. Liu, L. A. Fredin, T. C. B. Harlang, S. Lidin, J. Uhlig, V. Sundström, R. Lomoth, P. Persson, and K. Wärnmark, " $FeII$ hexa *n*-heterocyclic carbene complex with a 528 ps metal-to-ligand charge-transfer excited-state lifetime," *The Journal of Physical Chemistry Letters*, vol. 9, no. 3, pp. 459–463, 2018. PMID: 29298063.
- [29] L. A. Fredin, M. Pápai, E. Rozsályi, G. Vankó, K. Wärnmark, V. Sundström, and P. Persson, "Exceptional excited-state lifetime of an *iron(ii)*-*n*-heterocycliccarbene complex explained," *The Journal of Physical Chemistry Letters*, vol. 5, no. 12, pp. 2066–2071, 2014. PMID: 26270494.
- [30] Y. Liu, K. S. Kjær, L. A. Fredin, P. Chábera, T. Harlang, S. E. Canton, S. Lidin, J. Zhang, R. Lomoth, K.-E. Bergquist, P. Persson, K. Wärnmark,

- and V. Sundström, “A heteroleptic ferrous complex with mesoionic bis(1,2,3-triazol-5-ylidene) ligands: Taming the *mlct* excited state of *iron(ii)*,” *Chemistry – A European Journal*, vol. 21, no. 9, pp. 3628–3639, 2015.
- [31] M. Pastore, T. Duchanois, L. Liu, A. Monari, X. Assfeld, S. Haacke, and P. C. Gros, “Interfacial charge separation and photovoltaic efficiency in *fe(ii)*-carbene sensitized solar cells,” *Phys. Chem. Chem. Phys.*, vol. 18, pp. 28069–28081, 2016.
- [32] T. Duchanois, T. Etienne, C. Cebrián, L. Liu, A. Monari, M. Beley, X. Assfeld, S. Haacke, and P. C. Gros, “An iron-based photosensitizer with extended excited-state lifetime: Photophysical and photovoltaic properties,” *European Journal of Inorganic Chemistry*, vol. 2015, no. 14, pp. 2469–2477, 2015.
- [33] S. G. Shepard, S. M. Fatur, A. K. Rappé, and N. H. Damrauer, “Highly strained *iron(ii)* polypyridines: Exploiting the quintet manifold to extend the lifetime of *mlct* excited states,” *Journal of the American Chemical Society*, vol. 138, no. 9, pp. 2949–2952, 2016. PMID: 26863236.
- [34] K. S. Kjær, K. Kunnus, T. C. B. Harlang, T. B. Van Driel, K. Ledbetter, R. W. Hartsock, M. E. Reinhard, S. Koroidov, L. Li, M. G. Laursen, E. Biasin, F. B. Hansen, P. Vester, M. Christensen, K. Haldrup, M. M. Nielsen, P. Chabera, Y. Liu, H. Tatsuno, C. Timm, J. Uhlig, V. Sundstöm, Z. Németh, D. S. Szemes, Bajnóczi, G. Vankó, R. Alonso-Mori, J. M. Glowina, S. Nelson, M. Sikorski, D. Sokaras, H. T. Lemke, S. E. Canton, K. Wärnmark, P. Persson, A. A. Cordones, and K. J. Gaffney, “Solvent control of charge transfer excited state relaxation pathways in $[Fe(2,2 - bipyridine)(CN)_4]^2$,” *Phys. Chem. Chem. Phys.*, vol. 20, pp. 4238–4249, 2018.
- [35] L. Liu, T. Duchanois, T. Etienne, A. Monari, M. Beley, X. Assfeld, S. Haacke, and P. C. Gros, “A new record excited state 3mlct lifetime for metalorganic *iron(ii)* complexes,” *Phys. Chem. Chem. Phys.*, vol. 18, pp. 12550–12556, 2016.

- [36] M. Darari, E. Domenichini, A. Francés-Monerris, C. Cebrián, K. Magra, M. Beley, M. Pastore, A. Monari, X. Assfeld, S. Haacke, and P. C. Gros, “Iron(II) complexes with diazinylnhc ligands: impact of π -deficiency of the azine core on photophysical properties,” *Dalton Trans.*, vol. 48, pp. 10915–10926, 2019.
- [37] T. Harlang, Y. Liu, O. Gordivska, L. Fredin, C. Ponceca, P. Huang, P. Chábera, K. Kjær, H. Mateos, J. Uhlig, R. Lomoth, R. Wallenberg, S. Styring, P. Persson, V. Sundström, and K. Wärnmark, “Iron sensitizer converts light to electrons with 92% yield,” *Nature Chemistry*, vol. 7, no. 11, pp. 883–889, 2015.
- [38] J. K. McCusker, “Electronic structure in the transition metal block and its implications for light harvesting,” *Science*, vol. 363, no. 6426, pp. 484–488, 2019.
- [39] D. N Bowman, S. Mukherjee, L. J Barnes, and E. Jakubikova, “Linker dependence of interfacial electron transfer rates in *Fe(II)*-polypyridine sensitized solar cells,” *Journal of physics. Condensed matter : an Institute of Physics journal*, vol. 27, p. 134205, 03 2015.
- [40] “Fe^{II}/hexa n-heterocyclic carbene complex with a 528 ps metal-to-ligand charge-transfer excited-state lifetime,” vol. 9, pp. 459–463, 02 2018.
- [41] T. Duchanois, T. Etienne, M. Beley, X. Assfeld, E. A. Perpète, A. Monari, and P. C. Gros, “Heteroleptic pyridyl-carbene iron complexes with tuneable electronic properties,” *European Journal of Inorganic Chemistry*, vol. 2014, no. 23, pp. 3747–3753.
- [42] T. Duchanois, L. Liu, M. Pastore, A. Monari, C. Cebrian, Y. Trolez, M. Darari, K. Magra, A. Francés-Monerris, E. Domenichini, M. Beley, X. Assfeld, S. Haacke, and P. Gros, “NHC-Based Iron Sensitizers for DSSCs,” *Inorganics*, vol. 6, p. 63, June 2018.
- [43] O. S. Wenger, “Is iron the new ruthenium?,” *Chemistry – A European Journal*, vol. 25, no. 24, pp. 6043–6052, 2019.

- [44] B. Hou, Y. Du, X. Liu, C. Ci, X. Wu, and X. Xie, "Tunable preparation of highly dispersed $ni_xmn-ldo$ catalysts derived from $ni_xmn-lrhs$ precursors and application in low-temperature nh_3-scr reactions," *RSC Adv.*, vol. 9, pp. 24377–24385, 2019.
- [45] C. Förster, M. Dorn, T. Reuter, S. Otto, G. Davarci, T. Reich, L. Carrella, E. Rentschler, and K. Heinze, "Ddpd as expanded terpyridine: Dramatic effects of symmetry and electronic properties in first row transition metal complexes," *Inorganics*, vol. 6, no. 3, 2018.
- [46] I. M. Dixon, S. Khan, F. Alary, M. Boggio-Pasqua, and J.-L. Heully, "Probing the photophysical capability of mono and bis(cyclometallated) $fe(ii)$ polypyridine complexes using inexpensive ground state dft," *Dalton Trans.*, vol. 43, pp. 15898–15905, 2014.
- [47] S. Mukherjee, D. E. Torres, and E. Jakubikova, "Homo inversion as a strategy for improving the light-absorption properties of $fe(ii)$ chromophores," *Chem. Sci.*, vol. 8, pp. 8115–8126, 2017.
- [48] P. Chábera, Y. Liu, O. Prakash, E. Thyraug, A. El Nahhas, A. Honarfar, S. Essen, L. A. Fredin, T. C. Harlang, K. S. Kjær, *et al.*, "A low-spin $fe(iii)$ complex with 100-ps ligand-to-metal charge transfer photoluminescence," *Nature*, vol. 543, no. 7647, p. 695, 2017.
- [49] L. A. Büldt, X. Guo, R. Vogel, A. Prescimone, and O. S. Wenger, "A tris(diisocyanide)chromium(0) complex is a luminescent analog of $fe(2,2-bipyridine)_3^{2+}$," *Journal of the American Chemical Society*, vol. 139, no. 2, pp. 985–992, 2017. PMID: 28054486.
- [50] L. A. Büldt, X. Guo, A. Prescimone, and O. S. Wenger, "A molybdenum(0) isocyanide analogue of $ru(2,2-bipyridine)_3^{2+}$: A strong reductant for photoredox catalysis," *Angewandte Chemie International Edition*, vol. 55, no. 37, pp. 11247–11250, 2016.
- [51] S. Ferrere, "New photosensitizers based upon $[Fe(L)_2(CN)_2]$ and $[Fe(L)_3]$ (l = substituted 2,2'-bipyridine): yields for the photosensitization of TiO_2

- and effects on the band selectivity,” *Chemistry of Materials*, vol. 12, no. 4, pp. 1083–1089, 2000.
- [52] M. Yang, D. W. Thompson, and G. J. Meyer, “Charge-transfer studies of iron cyano compounds bound to nanocrystalline TiO_2 surfaces,” *Inorganic Chemistry*, vol. 41, no. 5, pp. 1254–1262, 2002. PMID: 11874363.
- [53] M. Yang, D. W. Thompson, and G. J. Meyer, “Dual pathways for TiO_2 sensitization by $Na_2[Fe(bpy)(CN)_4]$, journal = *Inorganic Chemistry*, volume = 39, number = 17, pages = 3738-3739, year = 2000, doi = 10.1021/ic000415l, note = PMID: 11196762, url = <https://doi.org/10.1021/ic000415l> , eprint = <https://doi.org/10.1021/ic000415l> ,”
- [54] S. Ferrere and B. A. Gregg, “Photosensitization of TiO_2 by $[FeII(2,2' - bipyridine - 4,4' - dicarboxylicacid)_2(CN)_2]$: band selective electron injection from ultra-short-lived excited states,” *Journal of the American Chemical Society*, vol. 120, no. 4, pp. 843–844, 1998.
- [55] S. Goberna-Ferrón, W. Y. Hernández, B. Rodríguez-García, and J. R. Galán-Mascarós, “Light-driven water oxidation with metal hexacyanometallate heterogeneous catalysts,” *ACS Catalysis*, vol. 4, no. 6, pp. 1637–1641, 2014.
- [56] E. P. Alsaç, E. Ülker, S. V. K. Nune, Y. Dede, and F. Karadas, “Tuning the electronic properties of prussian blue analogues for efficient water oxidation electrocatalysis: Experimental and computational studies,” *Chemistry – A European Journal*, vol. 24, no. 19, pp. 4856–4863, 2018.
- [57] S. Pintado, S. Goberna-Ferrón, E. C. Escudero-Adán, and J. R. Galán-Mascarós, “Fast and persistent electrocatalytic water oxidation by co-fe prussian blue coordination polymers,” *Journal of the American Chemical Society*, vol. 135, no. 36, pp. 13270–13273, 2013. PMID: 23978044.
- [58] M. Aksoy, S. V. K. Nune, and F. Karadas, “A novel synthetic route for the preparation of an amorphous co/fe prussian blue coordination compound with high electrocatalytic water oxidation activity,” *Inorganic Chemistry*, vol. 55, no. 9, pp. 4301–4307, 2016. PMID: 27074106.

- [59] T. G. UlusoyGhobadi, E. AkhuseyinYildiz, M. Buyuktemiz, S. SadighAkbari, D. Topkaya, İsci, Y. Dede, H. G. Yaglioglu, and F. Karadas, “A noble-metal-free heterogeneous photosensitizer-relay catalyst triad that catalyzes water oxidation under visible light,” *Angewandte Chemie International Edition*, vol. 57, no. 52, pp. 17173–17177, 2018.
- [60] T. G. Ulusoy Ghobadi, A. Ghobadi, M. Buyktemiz, E. Akhuseyin Yildiz, D. B. Yildiz, H. G. Yaglioglu, F. Karadas, Y. Dede, and E. Ozbay, “A robust precious metal-free dye-sensitized photoanode for water oxidation: Nanosecond long excited state lifetime via a prussian blue analogue,” *Angewandte Chemie International Edition*, vol. n/a, no. n/a.
- [61] M. Yamamoto, J. Föhlinger, J. Petersson, L. Hammarström, and H. Imahori, “A ruthenium complex–porphyrin–fullerene-linked molecular pentad as an integrative photosynthetic model,” *Angewandte Chemie International Edition*, vol. 56, no. 12, pp. 3329–3333, 2017.
- [62] M. Yamamoto, L. Wang, F. Li, T. Fukushima, K. Tanaka, L. Sun, and H. Imahori, “Visible light-driven water oxidation using a covalently-linked molecular catalyst–sensitizer dyad assembled on a TiO_2 electrode,” *Chem. Sci.*, vol. 7, pp. 1430–1439, 2016.
- [63] B. M. Pires, P. L. dos Santos, V. Katic, S. Strohauer, R. Landers, A. L. B. Formiga, and J. A. Bonacin, “Electrochemical water oxidation by cobalt-prussian blue coordination polymer and theoretical studies of the electronic structure of the active species,” *Dalton Trans.*, vol. 48, pp. 4811–4822, 2019.
- [64] A. A. Schilt, “Mixed ligand complexes of iron(II) and (III) with cyanide and aromatic di-imines,” *Journal of the American Chemical Society*, vol. 82, no. 12, pp. 3000–3005, 1960.
- [65] T. G. Ulusoy, A. Ghobadi, and A. K. Okyay, “Surface engineered angstrom thick ZnO -sheathed TiO_2 nanowires as photoanodes for performance enhanced dye-sensitized solar cells,” *J. Mater. Chem. A*, vol. 2, pp. 16867–16876, 2014.

- [66] A. Ghobadi, T. G. Ulusoy, R. Garifullin, M. O. Guler, and A. K. Okyay, “A heterojunction design of single layer hole tunneling ZnO passivation wrapping around TiO_2 nanowires for superior photocatalytic performance,” *Scientific reports*, vol. 6, p. 30587, July 2016.
- [67] A. A. Schilt, “Cyanide stretching frequencies of some mixed ligand complexes of iron, ruthenium, and osmium,” *Inorganic Chemistry*, vol. 3, no. 9, pp. 1323–1325, 1964.
- [68] Z. Kap and F. Karadas, “Visible light-driven water oxidation with a ruthenium sensitizer and a cobalt-based catalyst connected with a polymeric platform,” *Faraday Discuss.*, vol. 215, pp. 111–122, 2019.
- [69] F. S. Hegner, I. Herraiz-Cardona, D. Cardenas-Morcoso, N. López, J.-R. Galán-Mascarós, and S. Gimenez, “Cobalt hexacyanoferrate on $BiVO_4$ photoanodes for robust water splitting,” *ACS Applied Materials & Interfaces*, vol. 9, no. 43, pp. 37671–37681, 2017. PMID: 28975785.